A novel approach to scaling experimentally produced downburst-like impinging jet outflows

Djordje Romanic [a,b,*], Edoardo Nicolini [b], Horia Hangan [a], Massimiliano Burlando [b], Giovanni Solari [b]

[a] *Wind Engineering, Energy and Environment (WindEEE) Research Institute, Western University, 2535 Advanced Avenue, London, Ontario, N6M 0E2, Canada*
[b] *Department of Civil, Chemical and Environmental Engineering (DICCA), Polytechnic School, University of Genoa, Via Montallegro 1, 16145, Genoa, Italy*

ARTICLE INFO

ABSTRACT

Downbursts are intense thunderstorm winds that can be found in most, if not all, regions around the globe. An accurate experimental investigation of downburst winds requires the proper geometric and kinematic scaling between the model downburst (m) created in a wind simulator and the full scale downburst event (p). This study makes a threefold contribution to further understanding of downburst outflows. First, the article introduces a new scaling methodology for downburst outflows based on the signal decomposition techniques of p and m downburst wind records. Second, the study describes a large set of m downbursts produced in the WindEEE Dome simulator at Western University and critically discusses their similarity with a large set of p events detected in the Mediterranean. Third, using the proposed scaling methodology, this paper attempts to partially reconstruct two p downburst events recorded in Genoa and Livorno, Italy. In total, 17 p and 1400 m downburst outflows are investigated herein, which represents the largest database of p and m downbursts combined. The similarity between p and m downbursts is quantitatively demonstrated for both mean and fluctuating components of the flows. The scaling method is verified by accurately predicting the known anemometer height of p events using m downburst measurements.

1. Introduction

A proper physical scaling of highly transient winds such as downbursts and tornadoes has been an open question in wind engineering and meteorological communities for a long time (Simpson, 1969; Simpson and Britter, 1980; Lundgren et al., 1992; Xu and Hangan, 2008; Refan et al., 2014; Nasr-Azadani and Meiburg, 2016). The focus of this paper is only on the scaling of downburst winds. Rain and hail falling in the precipitation zone of thunderstorm produce a downdraft of cold air that impinges on the ground. For instance, in situations when the cloud base is high, the rain will fall through a deep column of unsaturated air which will result in its substantial cooling due to the evaporation of raindrops. Sometimes and in the case of high altitude clouds such as altocumulus, precipitation can completely evaporate resulting in so-called dry downburst (Wakimoto, 1985). As this cold and dense air reaches the ground, it spreads radially in a starburst pattern forming a gravity current. The cold downdraft and its radial spread close to the surface are known as the downburst. The near-surface winds in intense downbursts can be as high

as $75 \, \mathrm{m \, s^{-1}}$ (Fujita, 1990). Indeed, the studies by Fujita (1990) and Holmes (2002) showed that thunderstorm winds are the most damaging winds in North America and Australia & New Zealand, respectively. Similarly, Järvi et al. (2007), Solari et al. (2012) and Pistotnik et al. (2011), among others, demonstrated the destructive nature of downbursts across Europe.

The difficulty of scaling downbursts is altogether avoided if only full scale events are investigated without modelling their characteristics in wind chambers or numerical models (Burlando et al., 2017; Lompar et al., 2018). However, full scale measurements are limited by their spatiotemporal extent and the deeper investigation of the phenomena usually requires their physical or numerical simulations. In these cases, a great care needs to be taken to properly scale the model (m) to the reality (p). In this paper, we use the traditional fluid dynamics nomenclature where "m" stands for the model (e.g., physical simulation in the wind chamber) and "p" denotes the prototype (i.e., real event in the atmosphere). If the scaling is proper, the prediction of p conditions is possible from the m observations based on similitude. In order to ensure the

---

complete similarity between p and m, the following similarities must be satisfied (Potter et al., 2011): (1) geometric, (2) kinematic, and (3) dynamic similarity. Geometric similarity requires that the m has the same shape and scaled dimensions as the p. The kinematic scaling demands that the velocity ratio is a fixed constant between the p and m flows. Lastly, the dynamic similarity requires that the ratio of the p and m forces is constant throughout the flow. The focus of this article is only on geometric and kinematic scaling. It is important to notice the scales are related through:

$$\Lambda_L = \Lambda_v \cdot \Lambda_T, \qquad (1)$$

where $\Lambda_L = L_p/L_m$ is the length (L) scale, $\Lambda_v = V_p/V_m$ is the velocity (V) scale, and $\Lambda_T = T_p/T_m$ is the time (T) scale. The scaling ratios are often defined as m over p quantities, whereas this paper, for convenience (Section 2), defines it as the ratio of p over m variables.

In the traditional atmospheric boundary layer (ABL) tests conducted in wind tunnels, the length scales are of the order of 300:1 to 500:1, while the velocity scales are approximately 3:1 to 5:1 (Ho et al., 2005). The time scales are then calculated from Eq. (1) as: $\Lambda_T = \Lambda_L/\Lambda_v$ and they are around 1:100. For instance, 36 s in m scale represents approximately 1 h in the p scale. Therefore, the experimental data should also be sampled with at least 100 time faster rate than in full scale. Similarly, if the height of the ABL in full scale is 500 m then its equivalent in the wind tunnel is around 1–1.5 m. The methodology of scaling ABL winds finds its foundation in the definition of geostrophic and gradient velocities at the top of the ABL and their independence of the surface roughness. At the same time, the ABL scaling procedure also assumes the neutrally stratified atmosphere, stationary and Gaussian ABL winds, predominantly horizontal wind vector, and the ABL that is in equilibrium with the underlying surface. These assumptions are partly or fully invalid in the case of highly transient and three-dimensional downburst winds.

However, regardless of the scaling issues, physical simulations of downbursts are mainly still carried out through two established methodologies of their modelling in wind simulators. Gravity currents are one approach to experimentally simulate downbursts (e.g., Simpson, 1969, 1972; Charba, 1974; Lundgren et al., 1992; Linden, 2012; Jones et al., 2015), while the other approach is using impinging jets (Chay and Letchford, 2002; Xu and Hangan, 2008; McConville et al., 2009). Gravity currents are physically more realistic method to simulate downburst because in this case both p and m currents are driven by horizontal gradients of hydrostatic pressure due to the air density differences (Linden, 2012). Lundgren et al. (1992) proposed a method for scaling gravity currents to full scale downbursts using the equivalent spherical radius of p and m to define Λ_L and the characteristic time $T_0 = \sqrt{\Lambda_L \rho_a/(g\Delta\rho)}$ to determine Λ_T; where $\Delta\rho$ is the density difference between ambient air (ρ_a) and gravity current (ρ_{gc}), and g is the acceleration due to gravity. The remaining Λ_v can be obtained by using the rearranged Eq. (1). However, this approach is not often used in wind engineering studies due to the small velocities in the scaled gravity current outflows.

On the other hand, the impinging jet approach is suitable for producing higher velocities, but it partially lacks the full physical representation of the naturally occurring downbursts. From wind engineering point of view, however, thermodynamic properties and density differences between downburst and ambient air are less important than the mean and fluctuating velocity fields (Solari et al., 2015a). In this approach, the spatial structure of downburst is simulated by creating an impinging jet over the floor of a test chamber (e.g., Wood et al., 2001; Chay and Letchford, 2002; Xu and Hangan, 2008; McConville et al., 2009; Jesson and Sterling, 2018). Different approaches such as the modifications of traditional ABL wind tunnels have also been used to generate gust outflows but with limitations in representing the downburst vortex dynamics in three dimensions (Aboutabikh et al., 2019). Clearly, the density-difference scaling proposed by Lundgren et al. (1992) cannot be used in these cases and a new scaling methodology is needed.

As reported in Letchford et al. (2002), many downburst-like impinging jet experiments were conducted in the past considering different downdraft diameters, jet speeds and turbulence, as well as the jet descent distance to the wall (e.g., Bakke, 1957; Poreh et al., 1967; Letchford and Illidge, 1999; Wood et al., 2001; Chay and Letchford, 2002; Junayed et al., 2019). Wood et al. (2001) presented an empirical equation to describe the evolution of the radial velocity profile for an impinging jet flow over a flat surface. They showed some similarity among the velocity profiles obtained using their empirical equation, previously published laboratory tests, and full-scale data (Fujita, 1985; Hjelmfelt, 1988). Chay and Letchford (2002) assumed for their downburst simulations a geometric scale in the range 3500:1–3000:1 based on the full-scale observation of downbursts in Colorado (Hjelmfelt, 1988). Holmes and Oliver (2000) formulated an empirical model of horizontal wind speed in downburst outflows and found a good agreement with the full-scale data provided by Hjelmfelt (1988). Jesson and Sterling (2018) proposed a simple analytical model that satisfactory captured the spatiotemporal variability of downburst outflows produced in a wind simulator. The reported length scale of their downburst outflows in the University of Birmingham transient wind simulator of the order of $\Lambda_L = 1600$. Mason and Wood (2005) compared the structure of a pulsed impinging flow with the downburst recorded at the Andrews AFB (Fujita, 1985) using a velocity scale $\Lambda_v = 3.3$, and a length scale $\Lambda_L = 3250$. Kim and Hangan (2007) conducted numerical simulations of impinging jets for various Reynolds numbers and compared the results with full-scale data of a translating downburst (Gast and Schroeder, 2004). They determined the length and the velocity scales in terms of the impinging jet diameter and the initial jet velocity. Xu and Hangan (2008) investigated a large range of Reynolds numbers in experimentally produced impinging jet flows considering different boundary conditions (surface roughness, axial and radial confinements, and jet-to-surface distance) and inlet conditions. Further, McConville et al. (2009) proposed the velocity scaling of p and m downbursts using the ratio between the maximum horizontal outflow velocities of p and m events. They obtained the length scales in the range 700:1–1000:1 by comparing their experiments with the full scale event recorded at the Andrews AFB (Fujita, 1985). Junayed et al. (2019) conducted a parametric study of the flow field in large-scale downbursts in the Wind Engineering, Energy and Environment (WindEEE) Dome (Hangan, 2010) at Western University. They reported similar trends between the trajectories of the leading vortex in the p and m downbursts, with the parabolic curvature of the m trajectory being higher than in the p event (Wakimoto, 1982) and other experimental simulations (Walker et al., 1987; Mason et al., 2005). Very recently, Jesson et al. (2019) determined downburst scaling parameters using the Fourier periods from the Continues Wavelet Transform technique and a characteristics radial wind speed. However, the authors also acknowledged that a generally accepted scaling methodology for downburst outflows is currently not present.

Reviewing the above studies, an argument can be put forward that the current scaling methodologies generally compare a stationary (i.e., nontranslating) m impinging jet released in a calm environment of a wind simulator (i.e., no background ABL winds) against the real p downburst that is influenced by the presence of background ABL winds and storm motion, among other factors (e.g., surface roughness inhomogeneities, atmospheric stability, obstacles, etc.). Along those lines, this paper also investigates stationary m impinging jets without background ABL winds, but the study introduces a new approach for their scaling against p events. The proposed method is based on matching the statistical properties of p and m time series of measured wind speeds. Both time series are point measurements typically obtained by using anemometers for the p time series (De Gaetano et al., 2014), and Cobra probes, Pitot tubes or hot-wire anemometers for the m time series (Xu and Hangan, 2008). In the first step, the introduced scaling methodology is generically applied to a large set of p and m time series in order to assess the typical range of obtained scales in the deployed wind chamber. All p time series investigated in this paper are the product of the full scale measuring

campaigns "Wind and Ports" (Solari et al., 2012) and "Wind, Ports and Sea" (Repetto et al., 2018) that took place in the period 2009–2015 in the Mediterranean. The m time series are the result of a comprehensive set of downburst simulations in the WindEEE Dome in Canada. In the second step, two p events are partially reconstructed in order to evaluate the applicability of the method to physically replicate full scale data. The scaling model is derived in Section 2, while the p and m datasets are described in Section 3. The results of this research are presented in three subsections. Section 4.1 describes the similarities and differences between p and m time series, while Section 4.2 shows the scales of m events in the WindEEE Dome. Further, Section 4.3 validates the scaling model against two particular p events. The key conclusions and prospects for further research are summarized in Section 5.

2. Scaling methodology

The instantaneous wind speed (v) of a downburst event can be expressed as (Holmes et al., 2008; Solari et al., 2015b; Burlando et al., 2017):

$$v_s(t_s) = \bar{v}_s(t_s) + v_s'(t_s),\tag{2}$$

where the subscript s is either m or p, $t_s \in [0, \Delta T_s]$ is the time with ΔT_s being the length of either m or p velocity records, $\bar{v}_s$ is the slowly-varying mean speed, and v_s' is the residual turbulent fluctuations. For full scale events, it is common that ΔT_p is 10 min or 1 h (Burlando et al., 2018). If the wind record is stationary, as it is often in the case of ABL winds, then $\bar{v}_s(t_s) = \bar{v}_s$ and we retrieve the conventional Reynolds decomposition for stationary turbulent flow. The classical moving average filter with the averaging period T_s is commonly used to extract the moving mean from the instantaneous data (Choi and Hidayat, 2002; Holmes et al., 2008; Burlando et al., 2017):

$$\bar{v}_{s,i} = \frac{1}{T_s} \sum_{j=i}^{i+k_s-1} v_{s,j},\tag{3}$$

but nevertheless other methods exist too (McCullough et al., 2014). Here, $k_s = f_{a,s} \cdot T_s$ is the averaging moving window and $f_{a,s}$ is the anemometer/probe sampling frequency. For the p time series, the averaging window is (Solari et al., 2015a; Burlando et al., 2017):

$$T_p = 30 \text{ s}.$$

It is clear from Eq. (2) that the statistical properties of $\bar{v}_s(t_s)$ and $v_s'(t_s)$ highly depend on the choice of T_s. Other values for T_p have also been proposed such as 60 s (Choi and Hidayat, 2002), 32 s (Chen and Letchford, 2006), 40 s (Holmes et al., 2008), and 17 s and 34 s (Lombardo et al., 2014). It will be demonstrated later in this section that the proposed scaling method is fairly robust to the choice of T_p, so we proceed henceforth with fully adopting $T_p = 30$ s.

Further, the residual turbulent fluctuations, $v_s'(t_s)$, can be written as:

$$v_s'(t_s) = \sigma_{v,s}(t_s)\tilde{v}_s'(t_s),\tag{4}$$

where $\sigma_{v,s}$ is the slowly-varying standard deviation of v_s':

$$\sigma_{v,s,i}(t_s) = \sqrt{\frac{1}{T_s - 1} \sum_{j=i}^{i+T_s-1} \left(v'_{s,j}(t_s) - \bar{v}'_{s,j}(t_s)\right)^2}\tag{5}$$

where $\bar{v}'_{s,j}(t_s)$ is the average of this metric, and $\tilde{v}_s'$ is the reduced turbulent fluctuation. Using Eq. (4), we cast Eq. (2) in the form:

$$v_s(t_s) = \bar{v}_s(t_s)\left[1 + I_{v,s}(t_s)\tilde{v}_s'(t_s)\right],\tag{6}$$

where:

$$I_{v,s}(t_s) = \frac{\sigma_{v,s}(t_s)}{\bar{v}_s(t_s)}\tag{7}$$

is the slowly-varying turbulence intensity.

Furthermore, let us introduce the following two non-dimensional ratios (Solari et al., 2015a):

$$\gamma_s(t_s) = \frac{\bar{v}_s(t_s)}{\bar{v}_{\max,s}},\tag{8}$$

$$\mu_s(t_s) = \frac{I_{v,s}(t_s)}{\bar{I}_{v,s}},\tag{9}$$

where $\bar{v}_{\max,s}$ and $\bar{I}_{v,s}$ are the maximum value of $\bar{v}_s(t_s)$ and the average value of $I_{v,s}(t_s)$, respectively. Substituting Eqs. (8) and (9) into Eq. (6), the instantaneous velocity can be re-written as:

$$v_s(t_s) = \bar{v}_{\max,s}\gamma_s(t_s)\left[1 + \bar{I}_{v,s}\mu_s(t_s)\tilde{v}_s'(t_s)\right].\tag{10}$$

It is worth pointing out once again that all variables on the right-hand side of Eq. (10) are functions of T_s, including the constants $\bar{v}_{\max,s}$ and $\bar{I}_{v,s}$.

For a couple of downburst records—one being an p event and the other being an m event—we define the velocity scale (Λ_v) between these two time series as their ratio:

$$\Lambda_v(T_m) = \frac{v_p(t_p)}{v_m(t_m)}.\tag{11}$$

Note that Λ_v is only function of T_m since T_p is fixed.

Combining Eqs. (11) and (10), we obtain:

$$\Lambda_v(T_m) = \frac{\bar{v}_{\max,p}\gamma_p(t_p)}{\bar{v}_{\max,m}\gamma_m(t_m)} \cdot \frac{1 + \bar{I}_{v,p}\mu_p(t_p)\tilde{v}_p'(t_p)}{1 + \bar{I}_{v,m}\mu_m(t_m)\tilde{v}_m'(t_m)},\tag{12}$$

or, in short,

$$\Lambda_v(T_m) = M_v(T_m) \cdot F_v(T_m),\tag{13}$$

where

$$M_v(T_m) = \frac{\bar{v}_{\max,p}\gamma_p(t_p)}{\bar{v}_{\max,m}\gamma_m(t_m)},\tag{14}$$

$$F_v(T_m) = \frac{1 + \bar{I}_{v,p}\mu_p(t_p)\tilde{v}_p'(t_p)}{1 + \bar{I}_{v,m}\mu_m(t_m)\tilde{v}_m'(t_m)}.\tag{15}$$

At this point, it is important to clarify that the focus throughout this derivation is on the role of T_m in the scaling procedure, but clearly all quantities on the left hand side also depend on t_p and t_m, as the p and m time series have to be properly aligned. In addition, the m and p terms also depend on the height and radial distance from the downburst center. This dependency appears clearly in Sections 4.3.1 and 4.3.2. Therefore, formally $M_v = M_v(T_m, t_p, t_m, r_m)$, where r_m is the measurement position in respect to the downdraft center. The same holds for F_v.

Here, M_v represents the scaling between the mean flows whereas F_v is the scaling of the fluctuating part of the two velocity records. Using Eqs. (3) and (5), the numerators in Eqs. (14) and (15)) are readily available from full scale measurements. The relevant question to ask is therefore: What is the value of T_m that will provide the proper scaling between m and p time series? Here, we propose the following parametric approach to determine the value of T_m which will result in the proper velocity scale of the mean flows (M_v):

1. For the m time series, $v_m(t_m)$, assume a value of averaging window $T_m = T_{m,n}$, $n \in \mathbb{N}$ and $T_m \in [0, \Delta T_m]$.
2. For the given $T_{m,n}$ from Step 1, obtain $\bar{v}_{m,n}(t_{m,n})$, $\bar{v}_{max,m,n}(t_{m,n})$ and $\gamma_{m,n}(t_{m,n})$.
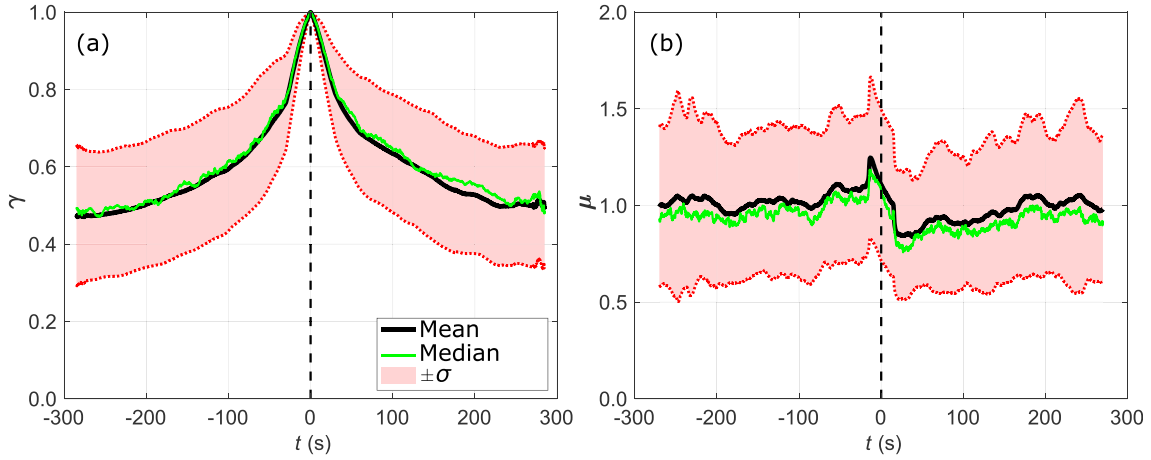
Fig. 1. (a) $\gamma_p(t_p)$ and (b) $\mu_p(t_p)$ functions from full scale 10-min downburst records (data from Zhang et al., 2017).

3. Calculate $M_{v,n}(T_{m,n})$ after aligning the $\gamma_{m,n}(t_{m,n})$ and $\gamma_p(t_p)$ time series in respect to the position of the velocity peak $\bar{v}_{max,m,n}(t_{m,n})$.

4. The proper value of M_v is the one that results in the lowest root-mean-square error (RMSE) between the two time series of $\gamma_p(t_p)$ and $\gamma_{m,n}(t_{m,n})$, i.e.:

$$\mathrm{RMSE}(T_{m,n}) = \sqrt{\frac{\sum_{n=0}^{N-1} \left[\gamma_p\left(t_p\right) - \gamma_{m,n}(t_{m,n}) \right]^2}{N}} \ , \tag{16}$$

where $N \in [0, \Delta T_m]$ is the maximum length of the interval considered around the velocity peak. A value of $\mathrm{RMSE}(T_{m,n}) = 0$ indicates that two time series $\gamma_p(t_p)$ and $\gamma_{m,n}(t_{m,n})$ have the exact same shape. Note that the amplitudes cannot differ since both time series are normalized with the maximum value, thus $\gamma_s|_{t_s=0} = 1$. Although we omit the longer notation, notice that formally $\mathrm{RMSE} = \mathrm{RMSE}(T_{m,n}, t_p, t_m, r_m)$.

5. Next, determine the lowest value of $\mathrm{RMSE}(T_{m,n})$, called $\mathrm{RMSE}_P(T_{m,P})$, where the subscript capital "P" stands for the "proper" scale, viz.:

$$\mathrm{RMSE}_P(T_{m,P}) = \min_{n_1, n_2, \ldots, N} \mathrm{RMSE}(T_{m,n}). \tag{17}$$

6. Obtain the value of $T_{m,P}$ that resulted in $\mathrm{RMSE}_P(T_{m,P})$, and determine $M_{v,P}$.

It is worth noting that throughout this iterative procedure the shape of $\gamma_p(t_p)$ does not change because $T_p = 30$ s is fixed, while the shape of $\gamma_{m,n}(t_{m,n})$ strictly depends on the choice of $T_{m,n}$. Solari et al. (2015a) and Zhang et al. (2017) investigated the shapes of γ_p and μ_p for more than 100 transient wind speed records measured in the Mediterranean (Solari et al., 2012) and preliminarily labelled as thunderstorm downburst. Using their data, we show the resulting γ_p functions in Fig. 1a. The mean γ_p in Fig. 1a (thick black line) nicely portrays the well-known signature of a downburst event through an abrupt ramp-up (i.e., part of downburst velocity record between the beginning of downburst and velocity peak) and decrease of the mean wind speed. In addition, the inner envelope of the diagram can be well approximated by the half-sine wave function (Kwon and Kareem, 2009). The variability around the mean γ_p (red shaded area) expressed through standard deviation (σ) shows that the spread around the mean γ_p increases by moving away from the velocity peak at $t = 0$ s. Fig. 1a shows a constant spread of around 25% around mean γ_p in the interval $t < 100$ s and $t > 100$ s. The standard deviation in the inner part of γ_p curves is much smaller. The median γ_p curve (green line) is similar to the mean γ_p curve indicating a Gaussian distribution of the γ_p samples.

The non-dimensional function associated with the turbulent nature of the flow, μ_p [Eq. (9)], is depicted in Fig. 1b using the data from Zhang et al. (2017). By demonstrating that both μ_p and its covariance are weakly dependent on time, Solari et al. (2015a) concluded that each μ_p is a sample of a (weakly) stationary process and therefore the value of $\bar{I}_{v,p}$ is weakly dependent on the choice of T_p. However, Solari et al. (2015a) and Zhang et al. (2017) also points out that μ_p should not be modelled as a fixed constant due to a small asymmetry with the respect to the mean value, which indicates non-Gaussian behavior of the function. This result is also confirm in Fig. 1b which shows a transient segment in μ_p around -50 s $< \mu_p < 50$ s. In this portion of the record, μ_p changes from being larger than 1 to below 1, which also demonstrates that $\bar{I}_{v,p} < I_{v,p}(t_p)$ for $t_p < 0$ s and vice versa for $t_p > 0$ s Therefore, both γ_p and μ_p are available for full scale data. This study will introduce their counterparts from the experimentally produced downbursts in a wind chamber. The transition from the maximum to the minimum values of μ_p occurs in approximately 100 s. In contrast to the variable spread around mean γ_p (Fig. 1a), the spread around mean μ_p is fairly constant over $\Delta T_p = 10$ min. The underlying distribution of μ_p is skewed to the right since the median μ_p is systematically below mean μ_p.

As expressed in Eq. (13), the overall velocity scale, Λ_v, is the product of the velocity scale of the mean flows, M_v, and the scaling of the fluctuating part of the flows, F_v. Since the transient nature of downburst flows is predominantly exerted through the changes of the mean flow for both p and m downbursts, we assume that the proper moving average period $T_{m,P}$ for the fluctuating part of the flows is the same as for the mean flow. Under this assumption, the fluctuating component of the velocity scale F_v is a stationary time series with the mean value around 1. This result indicates that by using $T_{m,P}$ as the averaging window of m data, the fluctuations in p and m time series are similar.

Knowing that the number of readings (k_s) within the moving window T_s is:

$$k_s = f_{a,s} \cdot T_s \ , \tag{18}$$

where $f_{a,s}$ is the sampling frequency of the instrument (the subscript "a" stands for "acquisition"), the proper time scale $\Lambda_{T,P}(T_{m,P})$ between the p and m time series is:

$$\Lambda_{T,P}(T_{m,P}) = \frac{f_{a,m}}{f_{a,p}} \frac{k_p}{k_{m,P}}. \tag{19}$$

As discussed in Section 1, recall that $f_{a,m} \gg f_{a,p}$ and since $k_{m,P} \gg k_p$, the model is in absolute terms weakly sensitive to the length of the averaging window of full scale data ΔT_p, in comparison to the variability of k_m. However, a case-by-case adopting value of ΔT_p could be implemented in

Table 1
Main characteristics of the *p* events considered in this study and properties of the monitoring network.

Location	Date	Hour (HH:MM:SS)	Anemometer code	Geographical coordinates (λ, ϕ) (°N, °E)	Height AGL (m)	$\hat{v}$ (m s^{-1})	$\bar{v}_{max}$ (m s^{-1})	α (°)
La Spezia	5 Jun 2011	14:50:00	SP.02	(44.110, 9.839)	13	23	18	231
Livorno	4 Sep 2011	15:35:30	LI.04	(43.541, 10.294)	20	23	21	242
		15:44:30	LI.03	(43.558, 10.290)	20	24	21	228
		15:45:00	LI.01	(43.570, 10.301)	20	23	21	256
		15:45:00	LI.05	(43.580, 10.319)	75	26	24	212
		15:52:00	LI.02	(43.583, 10.307)	20	24	19	261
La Spezia	25 Oct 2011	15:40:00	SP.03	(44.097, 9.858)	10	32	27	165
La Spezia	11 Apr 2012	07:20:00	SP.02	(44.110, 9.839)	13	30	23	196
La Spezia	19 Apr 2012	12:50:00	SP.03	(44.097, 9.858)	10	19	16	194
Genoa	30 Sep 2012	21:00:00	GE.02	(44.418, 8.777)	13.3	21	17	157
Livorno	1 Oct 2012	12:09:00	LI.03	(43.558, 10.290)	20	16	15	262
		12:11:00	LI.01	(43.570, 10.301)	20	18	16	277
		12:15:00	LI.05	(43.580, 10.319)	75	15	14	261
Livorno	26 Oct 2012	14:45:00	LI.01	(43.570, 10.301)	20	18	16	199
		14:45:00	LI.02	(43.583, 10.307)	20	16	11	241
		14:45:30	LI.03	(43.558, 10.290)	20	19	16	183
		14:45:30	LI.04	(43.541, 10.294)	20	21	19	205

the further development of this method.

At the end, the proper length scale ($\Lambda_{L,P}$) between the mean flows is calculated using Eq. (1), i.e.:

$$\Lambda_{L,P} = M_{v,P} \cdot \Lambda_{T,P}. \tag{20}$$

This approach of indirectly estimating a length scale from the explicitly calculated velocity and time scales from measured data was also adopted by Jesson et al. (2019).

3. Data

3.1. Full scale measurements

The full scale dataset used in this paper derives from the two European projects "Wind and Ports" (WP; Solari et al., 2012) and "Wind, Ports and Sea" (WPS; Repetto et al., 2018). In collaboration with the port authorities of Genoa, Savona, La Spezia, Livorno and Bastia, the projects' mission has been to establish a large monitoring network in the northern Mediterranean Sea with the purpose of collecting data for short- and medium-range wind forecasting in delicate areas such as commercial ports, as well as to create a statistical database of different wind types in the Tyrrhenian Sea. A total of 28 bi- or three-axial ultrasonic anemometers are installed throughout the ports. The anemometer sampling rate is 10 Hz (except for the anemometers in Bastia which are 2 Hz) and their precision is 0.01 m s^{-1} for wind speed and 1° for wind direction. Depending on the port, the anemometer heights vary from 10 to 84 m above ground level (AGL). Recently, the monitoring network has been upgraded with three weather stations and three LiDARs situated in Savona, Genoa and Livorno (Repetto et al., 2018). An exhaustive description of this field campaign is provided in Zhang et al. (2017). The wind measurements are transmitted to local servers located in each port from where 10-min statistical reports and raw data are further transferred to a central server situated in DICCA (Department of Civil, Chemical and Environmental Engineering, University of Genoa, Italy) for data validation, processing, and storage. Lastly, deploying a semi-automated separation procedure described in De Gaetano et al. (2014), the wind records are separated into three classes: (1) thunderstorms, (2) extra-tropical cyclones, and (3) intermediate winds.

As a result, over 250 strongly non-stationary thunderstorm wind records are available from the monitoring system (Zhang et al., 2017). For the present analysis we consider a total of 8 thunderstorm events captured by anemometers in Genoa, La Spezia and Livorno in the period from June 2011 to October 2012 (Table 1). Notice that some events are recorded with multiple anemometers making the total number of analyzed downburst records to 17 (i.e., *p* downburst records).
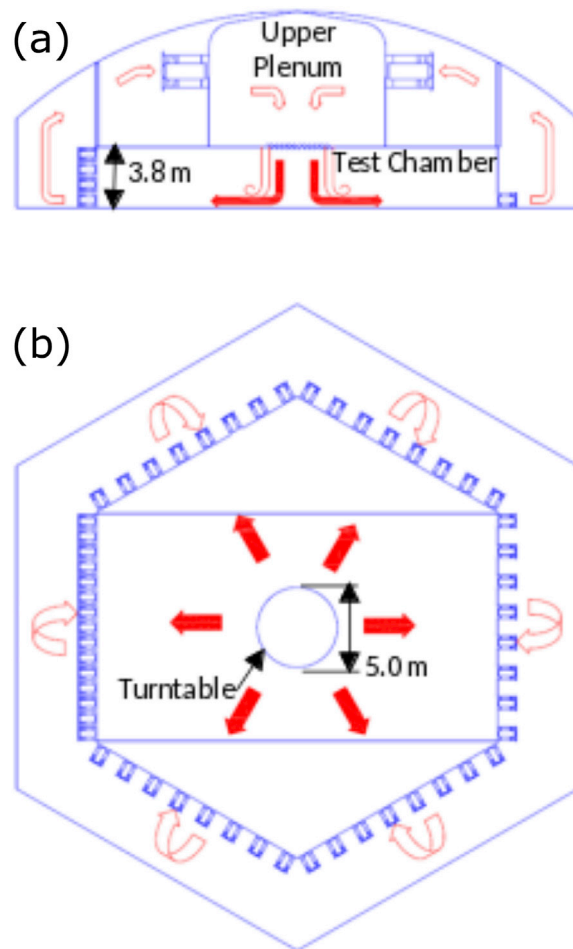
Fig. 2. (a) Side view and (b) top view of axisymmetric downburst mode of the WindEEE Dome.

Table 1 reports the main characteristics of downburst records analyzed in this paper. The strongest event analyzed in this study is recorded in La Spezia on 25 October 2011 with $\hat{v} = 32$ m s^{-1} at 10 m AGL. Similar to other events in the region (Burlando et al., 2017, 2018) the downburst was spawned above sea and moved towards the shore. The wind velocities are decomposed as described in Section 2 with all moving-mean quantities evaluated considering the averaging period of
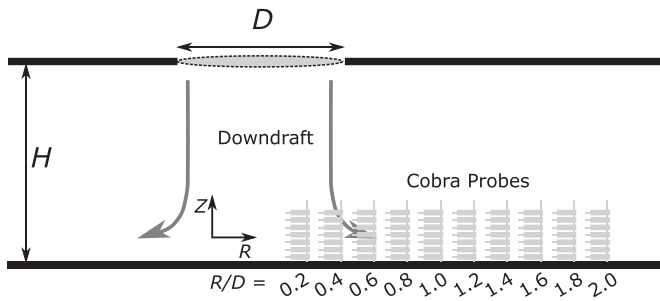
Fig. 3. Experiment setup in the WindEEE Dome.

$T_p = 30$ s. The variables such as γ_p and μ_p are derived from the 5-min windows centered around the time instant of $\bar{v}_{max}$.

3.2. Physical downburst simulations in the WindEEE Dome

The Wind Engineering, Energy and Environment (WindEEE) Dome (Hangan et al., 2017) at Western University in Canada is a three-dimensional wind testing facility designed to physically simulate non-stationary winds such as downbursts, tornadoes, gusts, separated flows, and sheared and veered flows, in addition to the straight and stationary ABL winds. The WindEEE Dome is a hexagonal chamber of 25 m in diameter surrounded by an outer return chamber of 40 m in diameter and the same hexagonal shape.

Downburst-like flows in the WindEEE Dome are generated as schematically depicted in Fig. 2. The 6 fans with a diameter of 2 m and located in the upper plenum are used to produce an impinging jet that runs through the bell mouth which connects the upper plenum with the testing chamber (Figs. 2 and 3). The process of creating an impinging jet starts by pressurizing the upper chamber using 6 fans and closing the louvers on the bell mouth. Once the pressure reaches the value of approximately 3.4 hPa above the pressure in the testing chamber, the bell mouth louvers are open and the air is released into the testing chamber.

The diameter of the experimentally produced downbursts investigated in this study is $D = 3.2$ m and their intensity expressed through the mean centroid jet velocity at the bell mouth exit is $V_{jet} = 8.9$ m s^{-1} (Romanic et al., 2019). This velocity is the result of approximately 20% of the maximum revolution per minute of the upper 6 fans.

Seven Cobra probes (developed by the Turbulent Flow Instrumentation Inc.) with the sampling frequency of 2500 Hz are used for velocity measurements in the WindEEE Dome. Their heights (Z) above the chamber floor were: 0.04, 0.10, 0.15, 0.20, 0.27, 0.42, and 0.50 m, but the values are provided as Z/D. These multi-hole pressure probes are designed to measure three components of incoming flow from a cone of $\pm45°$ in respect to the probe head. Cobra probe accuracy is ±0.5 m s^{-1} and $\pm1°$ yaw and pitch angles up to approximately 30% of turbulence intensity. The probes position in respect to downburst center is portrayed in Fig. 3. The velocity measurements are conducted at 10 radial positions spanning from $R/D = 0.2$ to $R/D = 2.0$ with an increment of 0.2, where R is the radial distance from the downdraft center. In accordance with the full scale downbursts that were formed above sea (see Section 3.1), the simulated downbursts in the WindEEE Dome impinged on the bare floor of the turntable without any roughness elements. With the aim to simulate as close as possible the transient nature of real downbursts, the time from opening to closure of bell mouth louvers was approximately 3–5 s. The experiments are independently repeated 20 times for each R/D position in order to better capture the turbulent nature of downburst outflows. In addition to 20 repetitions, the mean time series is obtained using an ensemble average:

$$v_m(t_{m,j}) = \frac{1}{M}\sum_{i=1}^{M} v_m^{(i)}(t_{m,j}),\tag{21}$$

where $v_m(t_{m,j})$ is the ensemble-average of the j th wind speed (v_m) reading in the time series ($j = 1, 2, ..., N$), N is the total number of readings, $i = 1, 2, ..., M$ is the ith member of the ensemble ($M = 20$), and t_m is the time. In total, 10 radial positions times 7 heights times 20 experiment repetitions per R/D resulted in 1400 experimentally produced downburst records (i.e., m downburst records).
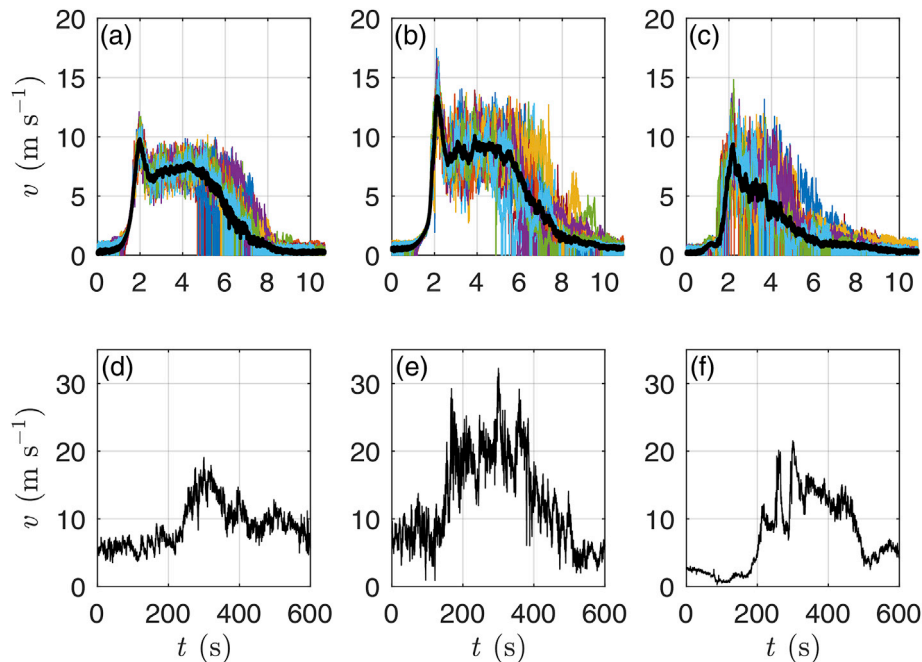

Fig. 4. Sample time series of experimentally produced downburst in the WindEEE Dome at $Z/D = 0.031$ and different R/Ds: (a) 0.6, (b) 1.2, and (c) 2.0. Colored lines are 20 repetitions of the same experiment while the thick black line is their ensemble average. Sample time series of three full scale events from Table 1 are shown in (d) 26 October 2012 (LI.01), (e) 11 April 2012 (SP.02), and (f) 30 September 2012 (GE.02).
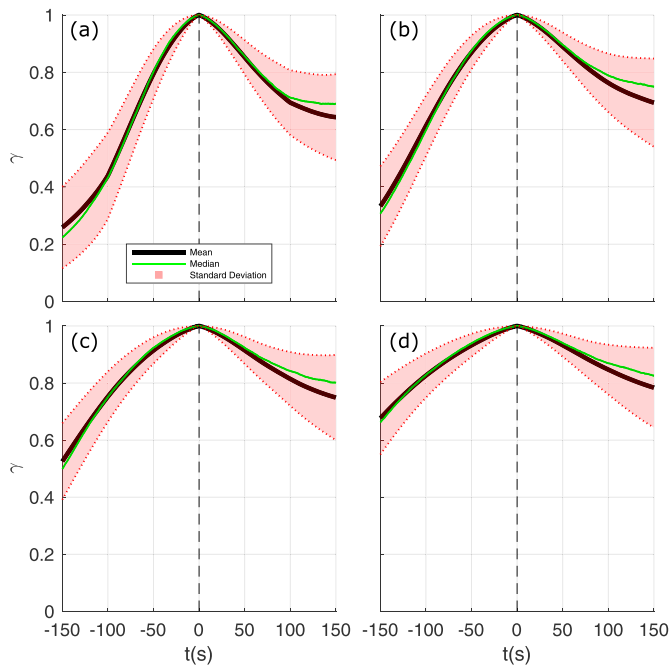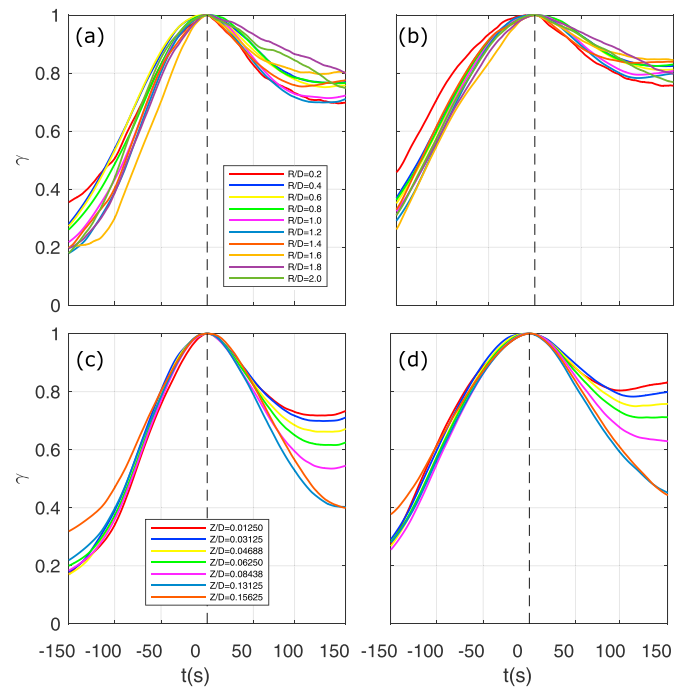
Fig. 5. $\gamma_m(t_m)$ functions of 1400 experimentally produced downburst records in the WindEEE Dome. Four panels correspond to different lengths of averaging window (T_m): (a) 0.4 s, (b) 0.6 s, (c) 0.8, and (d) 1.0 s. Equivalent full-scale time shown in abscissa.

Fig. 6. (a,b) Mean $\gamma_m(t_m)$ functions at different radial distances from downdraft center and at the height of $Z/D = 0.03125$ above ground using averaging window (T_m) of (a) 0.4 s and (b) 0.6 s. (c,d) Mean $\gamma_m(t_m)$ functions at different heights above ground and at the radial distance $R/D = 1.2$ using averaging window (T_m) of (c) 0.4 s and (d) 0.6 s.

4. Results

4.1. Similarity between m and p downbursts

Fig. 4 shows a few samples of m and p downburst time series. Before diving into quantitative comparisons between downburst records, Fig. 4 qualitatively demonstrates that both m and p time series possess the same overall features. The downburst peak that follows after a rapid velocity increase is present in both time series. A plateau of quasi-stationary velocity after the peak is also observed in m and p time series, but it seems to be more pronounced in the m cases. A steady decrease of velocity at the end of downburst is also accurately captured in the m records. The existence of background ABL winds prior to the p downbursts is the main difference between the experiments and reality. In the p records, the background winds prior to and after the downburst are approximately five times weaker than the downburst peak velocity. On the other hand, the m downbursts are generated without any background flow and therefore the velocities before and after the downburst reduce to zero. The absence of background winds in experimentally produced downbursts is one of the main challenges faced in the physical reconstruction of downburst outflows (e.g., Wood et al., 2001; Chay and Letchford, 2002; Letchford and Chay, 2002; Xu and Hangan, 2008; McConville et al., 2009). The WindEEE Dome has the capacity to combine background ABL and impinging jet flows (Romanic et al., 2019) and this combined mode is explored in a different study. The onus in this paper is on scaling and therefore we chose to limit ourselves to the impinging jet case only.

Fig. 5 shows mean (black line) and median (green line) of $\gamma_m(t_m)$ for all downburst records from the WindEEE Dome. The shape of both curves depends on the choice of the averaging period, T_m, in such a way that γ_m is steeper for smaller T_m and tends to flatten out with increasing T_m. That is, the slope of the mean γ_m decreases more than 3 times with increasing T_m from 0.4 s to 1.0 s. This spikiness of $\gamma_m(T_m)$ has a predominant influence on determining $T_{m,P}$ by minimizing the RMSEs in Eq. (17). In other words, the problem of finding the proper averaging time window, $T_{m,P}$, is usually reduced to the problem of determining the value of T_m

that gives the similar slope between the tails of γ_m and γ_p. The spread around mean (red shaded region) is larger after the velocity peak. This finding is also observed in Fig. 4a–c which shows that the ramp-up portion of the velocity record is more deterministic than the rest of the signal. In the m velocity records, there seem to be an absence of pronounced velocity fluctuations. The spread around the mean before and after the peak is similar if the longest averaging time is employed (Fig. 5d).

Since Fig. 5 presents the first set of γ functions from experimentally produced downbursts, it is beneficial to further compare their properties against the full scale γ functions previously shown in Fig. 1a. The spread observed between γ_ms and their deviation from the ensemble mean (thick black lines; Fig. 5) during the ramp-up segment is much smaller in the case of γ_ps (Fig. 1a). Fig. 4 also demonstrates that the fluctuations in the ramp-up segment of p events are more evident than that in m outflows. Fig. 1a shows the larger symmetry between two tails of the mean γ_p, as well as their collapse to a value of approximately 0.5 at the ends. In the m events, the left tail is always at the lower value than the right tail resulting in asymmetric γ_ms. However, the asymmetry decreases with increasing T_m and for $T_m = 1$ s the level of symmetry is similar as for the mean γ_p because by increasing averaging time we also constrain the analysis to the velocities around the peak. The relationship among mean γs and median γs is another similarity between γ_m and γ_p functions. In both cases, we observe that the mean and median γs are effectively the same prior to approximately $t = 100$ s. After that time, the median γ is higher than mean indicating a left-skewed distribution of individual γ functions. Analogous to γ_ps, the inner envelop of spread around mean γ_m can also be represented using a modified half-sine function proposed by Kwon and Kareem (2009). However, modifications to this simple model would have to be introduced due to the asymmetry γ_ms. It is important to point out that both γ_p and γ_m are heavy tailed on the left side due to the clear separation between the background ABL winds from downburst bell-like peak in the case of γ_p, and between the calm (zero velocity) before the downburst in the γ_m cases. The absence of winds prior to m
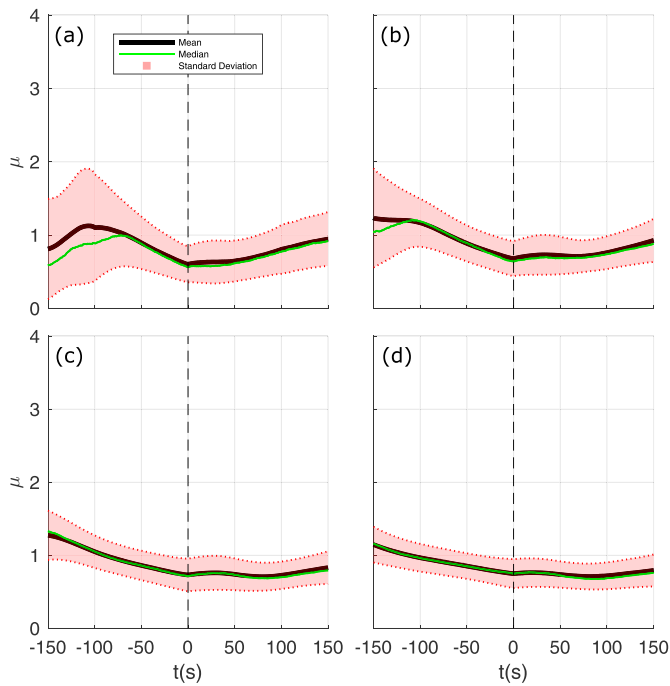
Fig. 7. Same as Fig. 5, but for $\mu_m(t_m)$. Four panels correspond to different lengths of averaging window (T_m): (a) 0.4 s, (b) 0.6 s, (c) 0.8, and (d) 1.0 s. Equivalent full-scale time shown in abscissa.

downbursts is likely the main cause of asymmetry in the tails of γ_ms.

A more systematic analysis of γ_m functions is presented in Fig. 6. Here, we investigate a dependency of γ_m functions on radial distance (R/D) from downdraft center (a,b) and height above ground (c,d). For the smallest averaging window and at the height of $Z/D = 0.03125$ (Fig. 6a), the largest values of γ_m functions in the ramp-up segment are observed at $R/D = 1.6$ and 1.8, whereas the strongest γ_ms (but less rapid velocity increase) are found for smaller R/Ds. While the similar observation is also valid for $T_m = 0.6$ s (Fig. 6b), it is not possible to fully generalize this finding since the pattern of larger-R/Ds-to-larger-γ_ms is not always preserved. For example, Fig. 6a shows that γ_m in the ramp-up segment at $R/D = 2.0$ is less rapid than that at $R/D = 1.6$ or 1.8. In principle, the same concussions can be drawn for the slowdown portion of γ_m functions; i.e., an absence of well-established pattern. For instance, the least steep to the steepest γ_m functions are observed at: 1.8, 2.0, 1.6, 0.4, 0.8, 0.6, 1.4, 0.2, 1.0 and 1.2. It should also be noted that there are many intersections between different γ_ms throughout the 5-min period around the peak.

Fig. 6c and d shows that γ_m functions are more dependent on height above ground than on R/D. At $R/D = 1.2$ and beyond $t = 100$ s, values of γ_ms decrease by increasing Z/D with an exception of the highest elevation ($Z/D = 0.15625$), which is slightly above $Z/D = 0.13125$. This pattern of γ_ms is another way of demonstrating the nose-shape profile of the mean velocity in a downburst outflow. At the same time, the ramp-up segments γ_m are very similar (excluding again the highest elevation prior to $t = -75$ s (Fig. 6c) and $t = -120$ s (Fig. 6d). This same clustering of γ_ms is also found in the first 50 s after the peak. This result indicates that the nose-shape profile might not be well-defined prior to and around velocity peak. Further study is needed in order to more comprehensively investigate a possible pattern of γ_ms for different Z/Ds and R/Ds, as well as different downdraft strengths and diameters. The spatiotemporal behavior of μ_m functions also needs to be addressed in future research.

Further, Fig. 7 shows the main statistics of $\mu_m(t_m)$ for all 1400 experimentally produced downbursts in the WindEEE Dome. Similar to γ_m in Fig. 5, μ_m also shows larger asymmetry between left and right tails for small T_ms. For $T_m = 0.4$ s and 0.6 s the function exhibits a periodic behavior, which diminishes after increasing T_m to 0.8 s and 1.0 s. Overall, the left tail is always at higher values than the right tail, which is further in accordance with the full scale results depicted in Fig. 1b, but the manifestation of this asymmetry pattern is not the same as in the p case. Namely, the function μ_p also shows asymmetry around the peak (Fig. 1b), but this asymmetry is shown as a step-like function around $t = 0$ s while the mean μ_m shows a period behavior (Fig. 7a and b) or monotonic decline (Fig. 7c and d). Another discrepancy between μ_m and μ_p are the below-unity and above-unity values at the peak velocity ($t = 0$ s), respectively. This result shows that when the velocity reaches the maximum value in an m outflow, then $I(t = 0$ s$) < \bar{I}$, which is usually not the case in p outflows (Fig. 1b) where turbulence intensity at the peak velocity stage is higher than the 10-min average value. Also, the median μ_p is always below the mean μ_p function which is not always the case and not well established in the m cases. Nevertheless, the observed asymmetry around the mean value observed in both p and m time series indicates that both flows are non-Gaussian (Solari et al., 2015a; Zhang et al., 2017; Hangan et al., 2019).

Lastly, the γ_p and μ_p functions of 17 analyzed p events in this paper are portrayed in Fig. 8. Notice that in comparison to Fig. 1, the functions are evaluated for a 5-min time interval centered on the peak velocity. The 5-min interval is more suitable for the scaling purposes in this paper due to the absence of the background winds in the m records. That is, opting for a 10-min interval results into including more non-downburst winds into the γ evaluation which does not have a physical correspondence in the m recods. In addition, Zhang et al. (2017) showed that a 5-min period is appropriate for very rapid downbursts, while longer periods should be
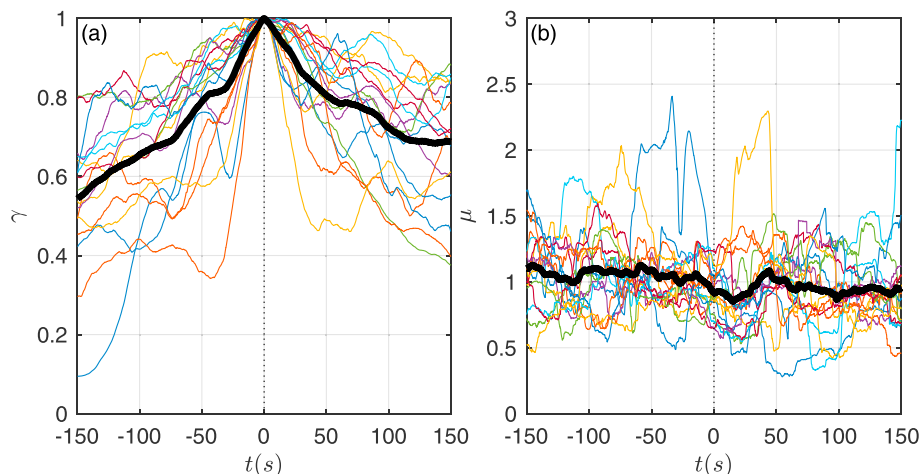

Fig. 8. Shapes of $\gamma_p(t_p)$ and $\mu_p(t_p)$ for 17 full scale downburst records analyzed in this study. Thick line represents the mean value.
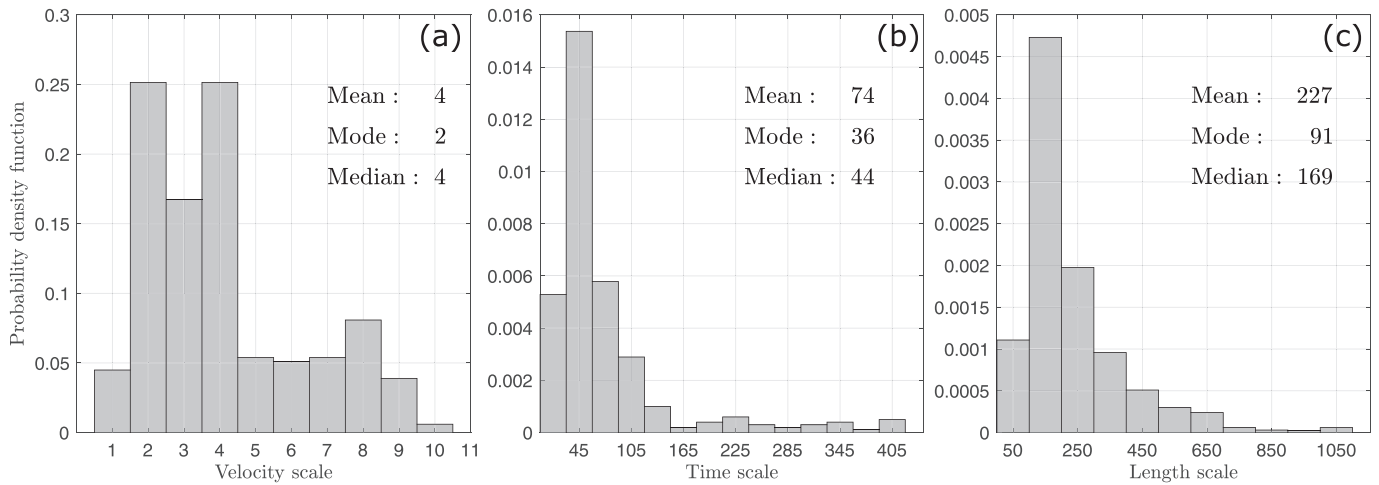
Fig. 9. (a) Velocity (mean flow), (b) time and (c) length scales of experimentally produced downbursts in the WindEEE Dome.

used for a slower downburst. Regardless of the time period of their evaluation (5 or 10 min), in both cases μ_p is a weak function of time, while γ_p is a highly transient process.

4.2. Scales of m downburst

Histograms of kinematic and geometric scales between p and m downburst records are shown in Fig. 9. The velocity (Fig. 9a) and time scales (Fig. 9b) are derived by comparing time series of p and m events, while the lengths scales (Fig. 9c) are afterwards computed from these two. The velocity scales of m downburst in the WindEEE Dome and p

events in the Mediterranean are typically between 2:1 and 4:1 (in about 70% of the cases). The most common velocity scale is 2:1. The time scales, on the other hand, are most frequently 36:1 with the mean time scale being 74:1. The large deviations of the mode from the mean are manifested as a non-Gaussian distribution of time scales of m records. Time scales around 100:1 and larger are also found for few events. Lastly, the combination of these two scales results in the length scales between the investigated cases to be 230:1 on average (Fig. 9c). The largest length scale found in this study is 1050:1. Similar range of scales was recently obtained by Junayed et al. (2019) in their study of downburst outflows in the WindEEE Dome.

Time scale is obtained by the virtue of deriving the velocity scale by
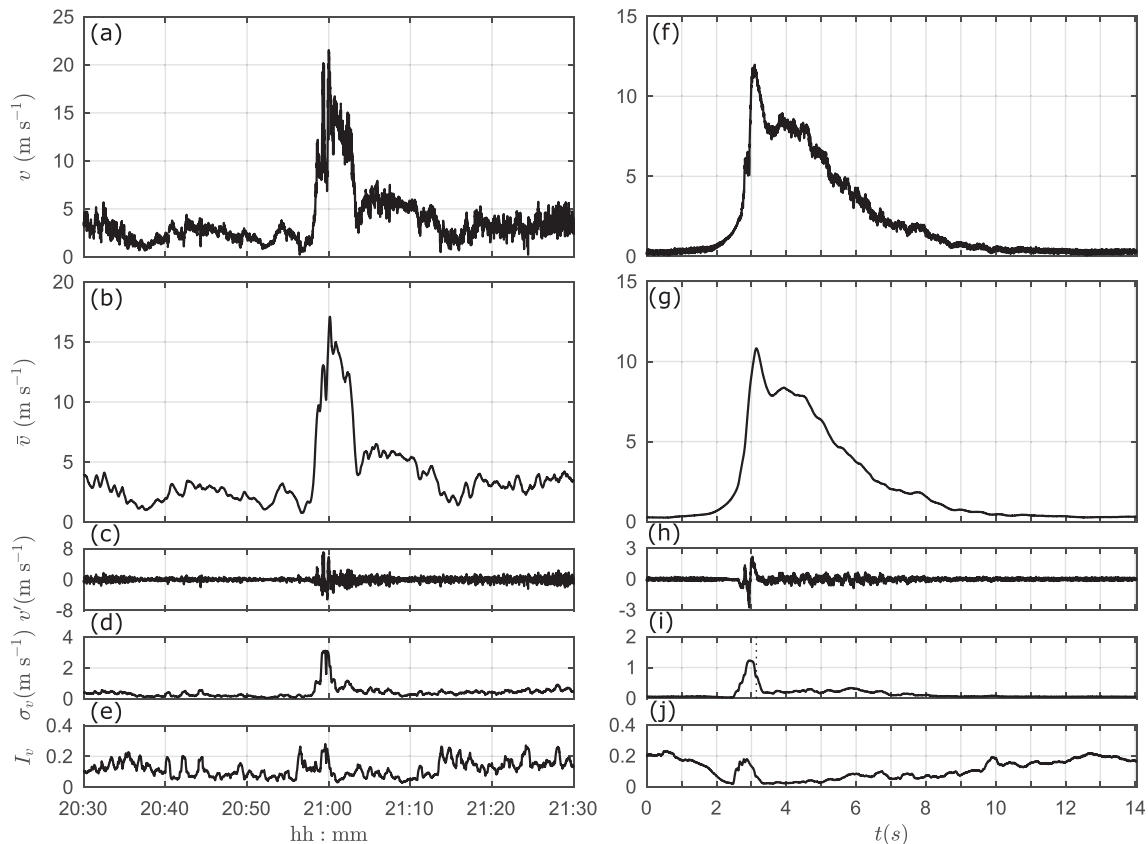

Fig. 10. (a)–(e): Decomposed wind velocity of the p downburst occurred in Genoa on 30 September 2012. (f)–(j): Decomposed wind velocity of the proper m downburst produced in the WindEEE Dome at $R/D = 1.4$ and $Z/D = 0.03125$.

comparing the γ functions of p and m downbursts. That is, these two scales are closely linked to each other in this approach. By increasing the averaging window, T_m, Eq. (14) shows that the velocity scale will increase since $\bar{v}_{max,m}$ decreases for larger T_ms. Similarly, if T_m is large, Eq. (19) demonstrates that the time scale decreases because k_m becomes large. Therefore, if the best matching between γ functions is obtained for large values of T_m, then the velocity scales will be large while the time scales will be small. We observe that the scales between the investigated p and m downbursts are overall positively skewed (Fig. 9).

It is worth mentioning that the derived scales shown in Fig. 9 are compatible with the possibility of reproducing them in a laboratory. This point is important for the investigation of downburst wind actions on structures; in which case the scaled model of the structure needs to be immersed in the flow. The geometric scales of the WindEEE Dome downburst are typically around 200:1 (Fig. 9c), which is similar to the geometric scales of many boundary layer wind tunnel tests (Ho et al., 2005). This level of similarity between the values of the geometric scales of the WindEEE Dome downbursts and the ABL winds in ABL wind tunnels holds also for the other two scales (Fig. 9a and b).

By comparing the γ functions centered on and normalized to the peak of the moving mean wind speed ($\bar{v}_{max,s}$), the method compares the segments of time series of the p and m events rather than comparing only two velocity values. By using the moving mean record rather than the instantaneous wind speed, the influence of random turbulence fluctuations on the scaling is minimized. It is worth noting that comparing two time series instead of two points is physically more meaningful and statistically more reliable approach. A single velocity value in p or m events, or both, can highly be influenced by random turbulence in the flow or by erroneous anemometer readings. Also, by investigating the shapes of self-similar γ functions the proposed method also compares different stages of downburst outflows by taking into account the properties of velocity ramp-up, peak, and slowdown segments in the p and m records.

At the end, the absence of an attempt to carry out dynamic scaling in this paper also deserves several comments. Xu and Hangan (2008) demonstrated that most features of impinging jet flows including the normalized mean velocity profiles are independent of Reynolds number after a critical value of Reynolds number. For a fixed H/D value, Xu and Hangan (2008) concluded that the radial variation of normalized maximum radial velocity is independent of Reynolds number. Their analysis was conducted for a range of Reynolds numbers from 23,000 to 190,000. Later, Junayed et al. (2019) investigated in details spectra of m downburst outflows from the WindEEE Dome simulator, as well as the Reynolds number dependency of these outflows. Their study reported Reynolds numbers between 1.82×10^6 and 4.24×10^6. While this range is very narrow, these values are higher than those analyzed in Xu and Hangan (2008). Moreover, Junayed et al. (2019) reported that the best match between p and m mean velocity profiles is found for $H/D > 1.0$ and $D = 3.2$ m, which is also the experiment setup used in the present study (Section 3.2). Finally, the proposed scaling method in this article operates only in time domain by comparing the dominant features of downburst outflows (e.g., γ_s and μ_s). A generalization of this approach that would in addition consider frequency domain features of two outflows could be considered in future.

### 4.3. Scaling applications and validation: partial reconstruction of p events

4.3.1. Genoa, 30 September 2012

The first in-depth analyzed p event in this study is measured in Genoa (Fig. 10a). On 30 September 2012, the anemometer positioned at 13.3 m AGL recorded a downburst event with a 1-s velocity peak of $\hat{v} = 21$ m s^{-1} around 21:00 UTC (Coordinated Universal Time). Similar to the majority of downbursts in that region (Burlando et al., 2018), this event also originated above sea and moved inland (Table 1). Fig. 10a shows that the background winds prior to and after the downburst event are below 5 m s^{-1}. This downburst is characterized with a very rapid

Table 2
Pearson correlation coefficient between instantaneous velocity records (r_v) and γ functions (r_γ) from Genoa and Livorno (LI.01) events. All records aligned to $t_s = 0$ s.

|	Genoa	Livorno
r_v	0.759	0.869
r_γ	0.937	0.936
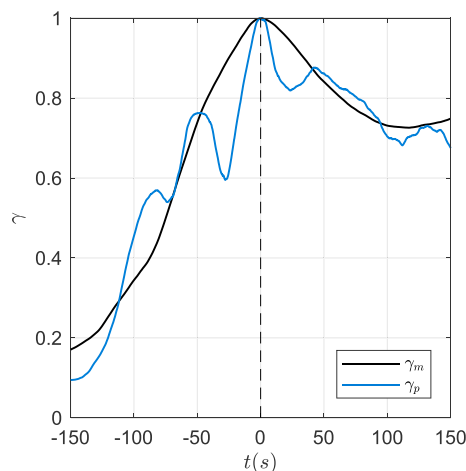
Fig. 11. Comparison of γ functions for the p downburst that occurred in Genoa, 30 September 2012, and the proper m downburst simulated in the WindEEE Dome at $R/D = 1.4$ and $Z/D = 0.03125$. The abscissa shows the p time.

ramp-up that occurred around 21:00 UTC and the duration of the main peak is about 10 min. Despite the longer duration of this m event, the γ functions are still compared for a time window of 5 min around the peaks (full-scale time equivalent) due to the rapid ramp-up of the m downburst and the lack of ABL winds prior to downburst in the laboratory conditions. Increasing the time window to 10 min would incorrectly include the Cobra probe noise prior to p downburst into the comparison. This issue is further discussed in Section 4.1.

Fig. 10b–e shows decomposed velocity signal over the time interval of $\Delta T_p = 1$ h using the moving average window of $T_p = 30$ s. The slowly-varying wind speed, $\bar{v}_p$, maintains a similar trend as the instantaneous wind velocity, v_p, characterized by rapid ramp up and showdown phases. That is, $\bar{v}_p$ depicts the mean characteristics of the downburst outflow. The remaining three graphs of the p event—namely, the panels (c), (d), (e)—describe the turbulent nature of the flow. Notice that the higher turbulence fluctuations are observed at the time instants around the downburst peak (Solari et al., 2015a; Burlando et al., 2017).

Fig. 10f–j portrays decomposed velocity of the proper m record that corresponds to the Genoa p event, while Table 2 shows the correlation between instantons velocity signals (Fig. 10a,f) expressed through the Pearson correlation coefficient (r). The applied decomposition methodology is the same as for the p events (Hangan et al., 2019). Before going into the quantitative comparison of γ functions between p and m records, Fig. 10 shows qualitative similarity between the two time series with the ramp-up portion, the peak and the quasi-steady segment after the peak being observed in both records. The main difference between the time series is in the more abrupt slowdown of velocity in the p case. Also, the moving turbulence intensity in the m record is smaller than in the real downburst. The same pattern is observed in the other two variables that describe turbulence fluctuations; namely $\sigma_{v,m}$ and v'_p.

Fig. 11 shows the comparison between γ_p of the Genoa downburst and γ_m from the WindEEE Dome. The similarity between γ functions is the best at $Z/D = 0.03125$ with an RMSE $= 0.0896$ and $r_\gamma = 0.937$ (Table 2). The main difference between γ functions is the increased level of
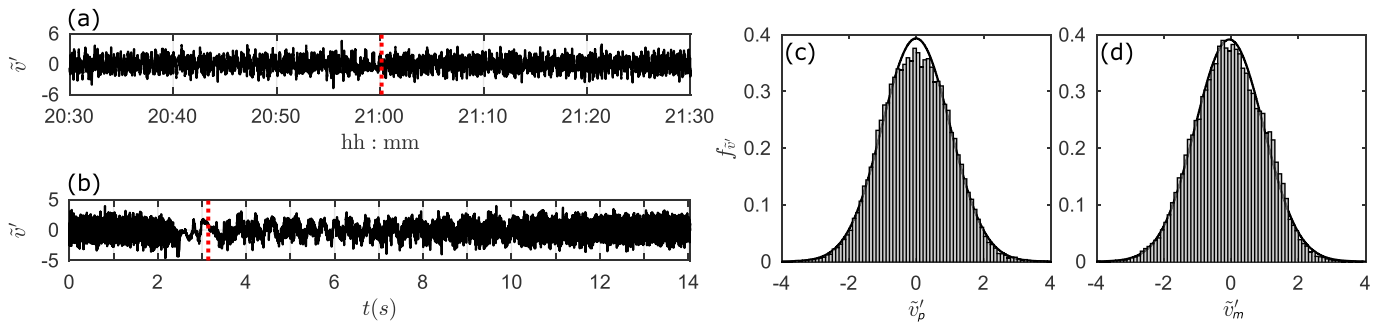
Fig. 12. (a–c) p downburst from Genoa, 30 September 2012, and (d)–(f) the proper m downburst simulated in the WindEEE Dome at $R/D = 1.4$ and $Z/D = 0.03125$. (a,d) Reduced turbulent fluctuation $\tilde{v}$'s. (b,e) Histograms of $\tilde{v}$ fitted with a Gaussian distribution. The vertical red (dashed) line in (a) and (b) indicate the time instant of peak velocity. Skewness (m_3) and kurtosis values (m_4) shown in (c) and (d). (For interpretation of the references to colour in this figure legend, the reader is referred to the Web version of this article.)
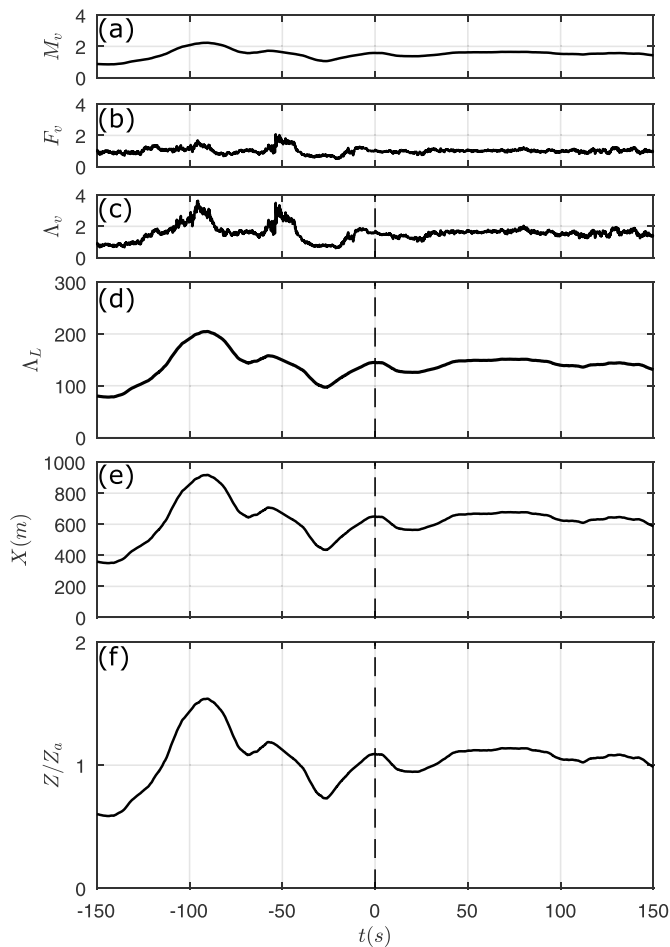
Fig. 13. (a) Mean velocity scale, (b) fluctuating velocity scale and (c) overall velocity scale part [product of (a) and (b)] between p downburst from Genoa, 30 September 2012, and the proper m record from WindEEE Dome. Panels (d), (e), and (f) show respectively the length scale, the estimated radial distance of the p downburst center from the anemometer GE.02, and the estimated height of the anemometer GE.02.

smoothness of γ_m. In general, for all the 17 cases analyzed, the γ_m function is always smoother than γ_p because the number of readings that enters the moving mean window in the p cases ($k_{m,P}$) is much larger in comparison to k_p. Secondly, the WindEEE Dome experiments seem to create a ramp-up segment of the m velocity time series with a deterministic character whereas their p counterparts are random in nature. In particular, as shown in Figs. 4 and 10, the turbulent fluctuations during

the ramp-up segment of the p time series are more pronounced than in the m records. This may be explained by pointing out that all m downbursts are released into the same calm environment of the WindEEE Dome testing chamber and the ramp-up portion of the signal represents the first encounter between the downburst outflow and the calm ambient air. This situation does not hold for the p events where the magnitude of turbulent fluctuations is similar throughout the whole downburst.

Fig. 12 is a comparison between the reduced turbulent fluctuation $\tilde{v}$' and the associated probability density function, $f_{\tilde{v}}$ of two p and m records from Fig. 10. While $\tilde{v}$' in the p event is a stationary Gaussian process, the m record shows departures from statistical stationarity and randomness of the signal in the region around the downburst ramp-up and the peak. This characteristics of $\tilde{v}'_m$ is also manifested through the larger departure of skewness (m_3) and kurtosis (m_4) from the Gaussian values of 0 and 3, respectively (Fig. 12d).

The time dependent scaling between p and m downbursts is portrayed in Fig. 13. After approximately 50 s, the mean velocity scale, $M_v(T_m)$, becomes fairly constant and weakly oscillates around $M_v = 2$ (i.e., the mean velocity scale between p and m records is 2:1). The initial oscillations in $M_v(T_m)$ are due to the presence of background ABL winds in the p record coupled with their absence in the m time series (Fig. 11). Similar to all other events analyzed in this paper, the fluctuating part of the velocity scale, $F_v(T_m)$, is almost constant and equal to 1:1. For determining either length or time scales, the $F_v(T_m)$ term is omitted since it is governed by turbulence and therefore relevant only for the velocity scaling—namely, it is physically meaningless to have fluctuating time or length scales.

The next important step is to validate the proposed scaling method. After calculating length scales in Fig. 13d, this information can in principle be used to estimate the height of the anemometer GE.02 in Genoa, which, of course, is already known to be at 13.3 m AGL (Table 1). The effectiveness of the method can be inferred by comparing the real height of anemometer with the calculated anemometer height ($Z_{a,p}$):

$$Z_{a,p} = \Lambda_L \cdot Z_{a,m}, \qquad (22)$$

where $Z_{a,m}$ is the height of the Cobra probe that recorded the proper m record. The results portrayed in Fig. 13f show a good match between $Z_{a,p}$ and the real height of anemometer GE.02 at 13.3 m AGL (Table 1). Once again, the oscillations in the first approximately 50 s should not be taken into consideration in this analysis as they are the result of the mismatch between the background ABL winds in the p record and a zero velocity in the m record prior to downburst. Excluding this segment, the $Z_{a,p}$ values in Fig. 13f are at approximately 13 m AGL throughout the time series, which matches the real anemometer height and hence validates the methodology (at least for this event).

Furthermore, using the same line of reasoning it is also possible to evaluate the radial position of the p downburst center (X) in respect to the anemometer location as:
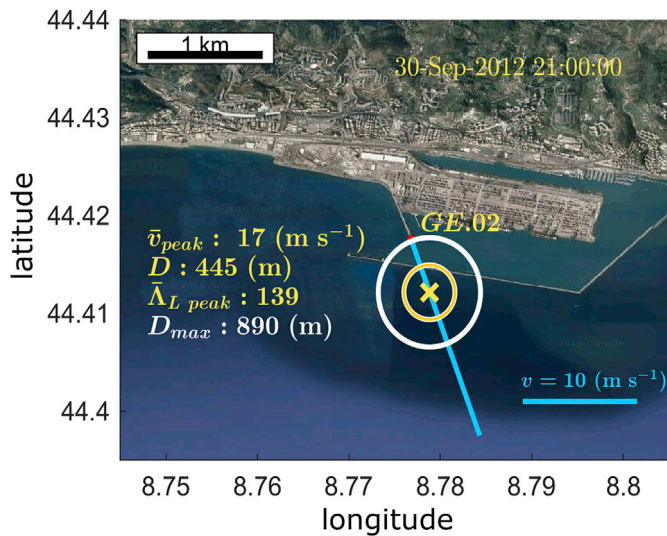
Fig. 14. Estimated position of the p downburst center (yellow $\times$) at the time instant of the peak velocity (Genoa, 30 September 2012). The red dot is anemometer position, D is the estimated downburst diameter (yellow circle) while D_{max} is the estimated distance between downburst center and the maximum wind speed in downburst outflow (white circle). The blue line indicates wind speed and direction at the time instant of peak velocity. (For interpretation of the references to colour in this figure legend, the reader is referred to the Web version of this article.)

$$X = \Lambda_L \cdot R, \tag{23}$$

where R is the radial distance from m downburst center to the Cobra probe that recorded the proper downburst record. Excluding the unreli-

able segment of the time series (i.e., first ~50 s in Fig. 14e), it seems that the p downburst was located approximately 600 m from the anemometer GE.02 at the time when the anemometer measured the peak velocity. The distance is unchanged in the next 2 min.

By using the wind direction at the time of the peak (Table 1), we further estimate the azimuthal location of the p downburst center in relation to the anemometer GE.02. The results are shown in Fig. 14. The estimated downburst diameter (yellow circle) derives directly from the length scale as: $D_p = \overline{\Lambda}_{L\,peak} \cdot D_{m,P}$, where $\overline{\Lambda}_{L\,peak}$ is the moving mean length scale at the peak instant, and $D_{m,P}$ is the diameter of the proper m downburst in the WindEEE Dome ($D_{m,P} = 3.2$ m). At the same time, it is possible to estimate the radius of the maximum velocity in the p event (white circle in Fig. 14) at the height of the anemometer by finding the radius of the maximum velocity in the m downburst. This partial reconstruction of the p event shows that the downburst might occurred about 900 m south-southeast from the anemometer and that the anemometer was located very close to the position of the maximum outflow velocity in the event.

This method can further be validated against the typically deployed velocity and time scaling (Mason and Wood, 2005; Kim and Hangan, 2007; McConville et al., 2009) where the velocity scale is simply the ratio of 1-s peak wind speeds and the time scale is the ratio of downburst ramp-up times in p and m records. The ratio of 1-s peaks $\hat{v}_p/\hat{v}_m = 21.0/11.5 = 1.82 \approx 2$ confirm the velocity scales obtained using the novel approach (Fig. 14). Advantages of the proposed scaling approach over this simple point-to-point velocity ratio have been previously discussed in Section 4.2. Similarly, the duration of the downburst peak in the p record is approximately 65 times longer than the m downburst (Fig. 10).

4.3.2. Livorno, 1 October 2012

The second partially reconstructed event is recorded in Livorno on 1 October 2012. This event was investigated in details in the recent study
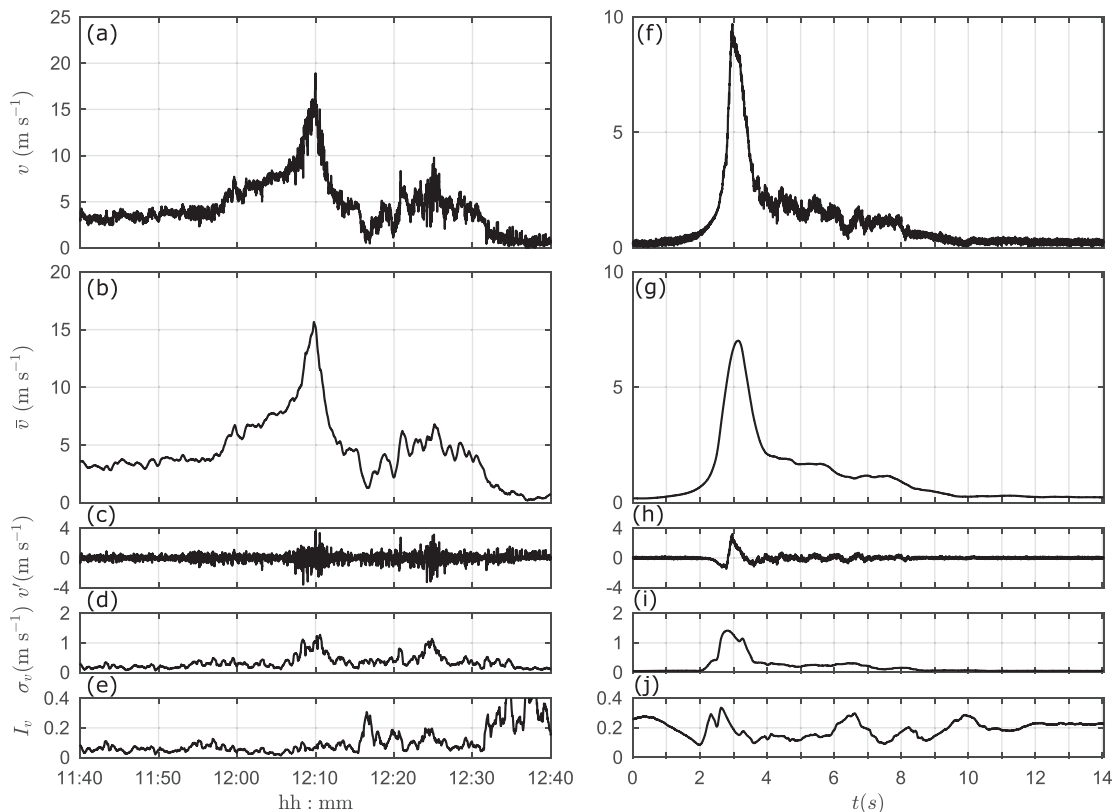
Fig. 15. (a)–(e): Decomposed wind velocity of the p downburst occurred in Livorno on 1 October 2012 for the anemometer LI.01. (f)–(j): Decomposed wind velocity of the proper m downburst produced in WindEEE Dome at $R/D = 1.4$ and $Z/D = 0.13125$.
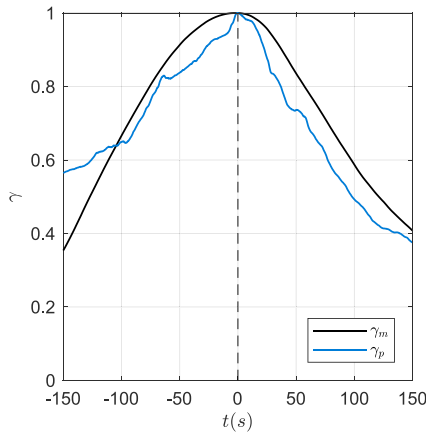
Fig. 16. Comparison of γ functions for the p downburst that occurred in Livorno, 1 October 2012, (anemometer LI.01) and the proper m downburst simulated in the WindEEE Dome at $R/D = 1.4$ and $Z/D = 0.13125$.

by Burlando et al. (2017). The downburst was recorded by three anemometers located in the Livorno port area and Burlando et al. (2017) demonstrated that this wet downburst advanced from sea towards land. The event was first captured by the anemometer LI.03 and the recorded maximum velocity was $16 \, \mathrm{m \, s^{-1}}$ at 12:09 UTC. Two minutes later the wind velocity peak $\hat{v} = 18 \, \mathrm{m \, s^{-1}}$ was observed by anemometer LI.01 (Fig. 15a), and at 12:15 UTC by anemometer LI.05 ($\hat{v} = 15 \, \mathrm{m \, s^{-1}}$). Using satellite and radar observations, Burlando et al. (2017) showed that the thunderstorm cloud had predominantly northward trajectory, which is also in accordance with the successive capturing of the peak velocities by anemometers LI.03, LI.01 and LI.05, in respective order. The partial reconstruction of this event is carried out for all three anemometers, but this paper shows in-depth results for the anemometer LI.01 (Fig. 15a–e) for the sake of shortness.

Decomposed velocity from the anemometer LI.01 is portrayed in Fig. 15b–e. The slowly-varying mean velocity (Fig. 15b) resembles the typical shape of a downburst event while the velocity fluctuations v_p' are approximately 3 times larger in the downburst peaks than in the rest of the record. In contrast to the Genoa downburst (Fig. 10a–e), where the pronounced fluctuations were associated only with the first downburst peak, the fluctuations in the Livorno events where similar in the first and second downburst peaks. This discrepancy might be due to the different life stages of these two downbursts (Wakimoto, 1982), as well as due to different measuring heights of anemometers in Genoa and Livorno, among other possibilities.

Fig. 15f–j shows the measured and decomposed velocity records of the proper m downburst in the WindEEE Dome for the p time series from Livorno downburst. Qualitatively, several differences between p and the
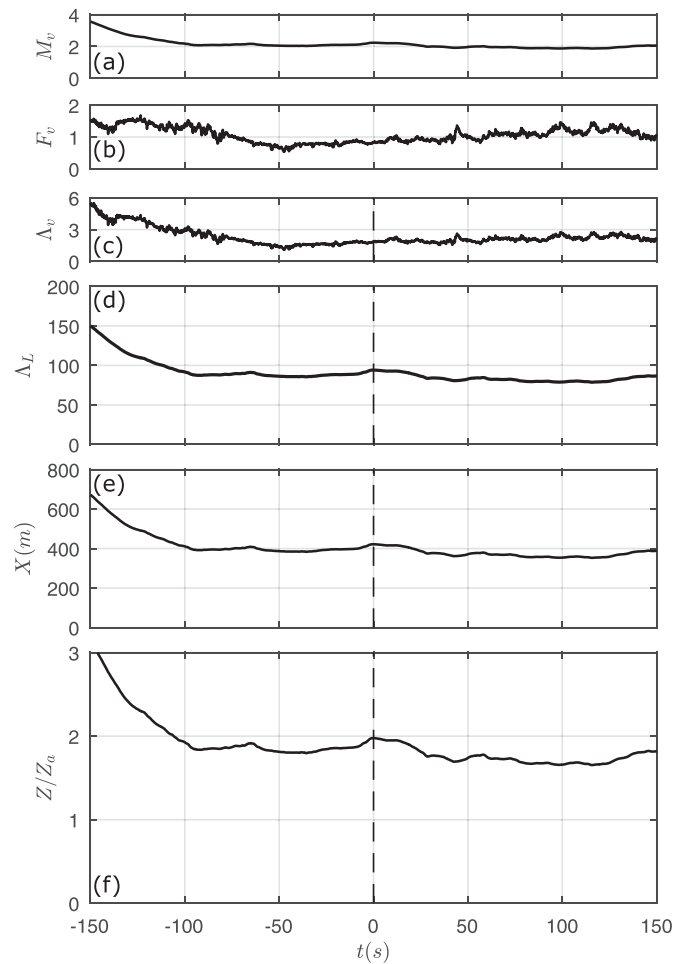

Fig. 18. (a) Mean velocity scale, (b) fluctuating velocity scale and (c) overall velocity scale part [product of (a) and (b)] between p downburst from Livorno, 1 October 2012 (anemometer LI.01), and the proper m record from WindEEE Dome. Panels (d), (e), and (f) show respectively the length scale, the estimated radial distance of the p downburst center from the anemometer LI.01, and the estimated height of the anemometer LI.01.

proper m records exist. First, the steady increase of wind speed prior to the first downburst peak in the p event is not observed in the m record. This mild increase of wind speed is sometimes referred to as a gust front and its existence is thought to be due to the interaction between thunderstorm and the ABL winds (Mahoney, 1988). Since the m experiments in the WindEEE Dome were performed without ABL winds, this segment of the time series is absent in the m record. It is worth pointing out that this feature of the time series is absent in some full scale events too (e.g.,
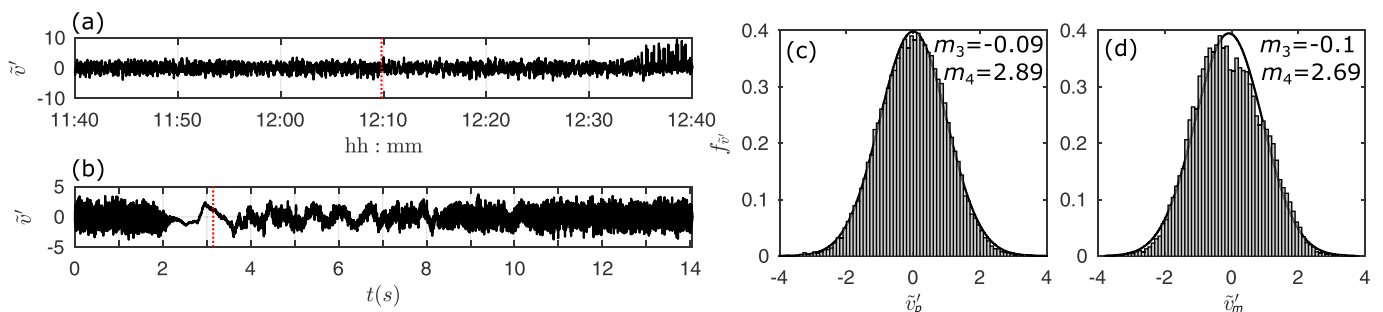

Fig. 17. (a–c) p downburst from Livorno, 1 October 2012 (anemometer LI.01), and (d)–(f) the proper m downburst simulated in the WindEEE Dome at $R/D = 1.4$ and $Z/D = 0.13125$. (a,d) Reduced turbulent fluctuation $\tilde{v}$'s. (b,e) Histograms of $\tilde{v}$ fitted with a Gaussian distribution. The vertical red (dashed) line in (a) and (b) indicate the time instant of peak velocity. Skewness (m_3) and kurtosis values (m_4) shown in (c) and (d).
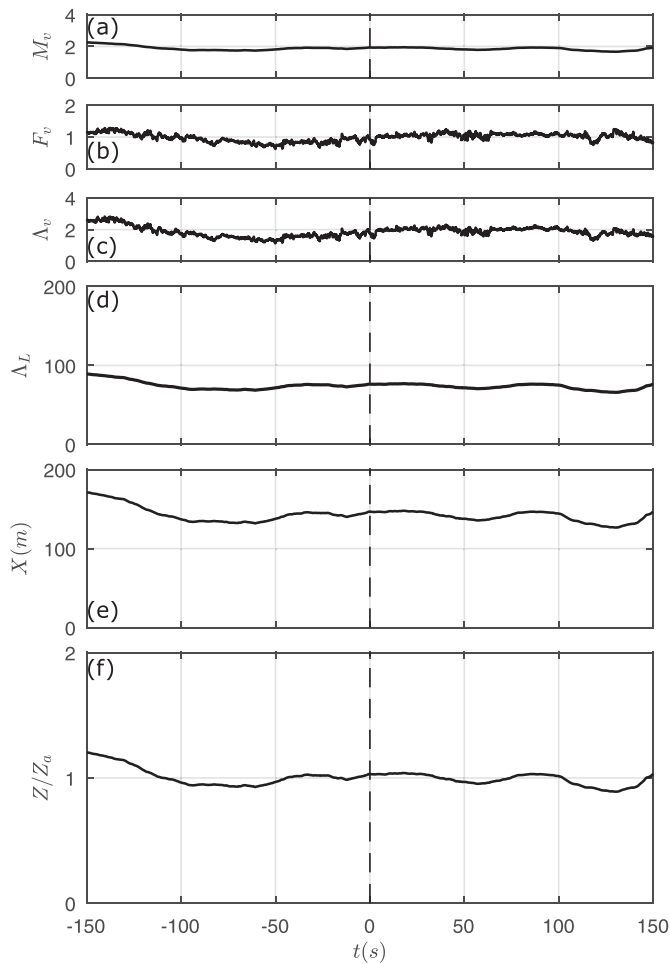
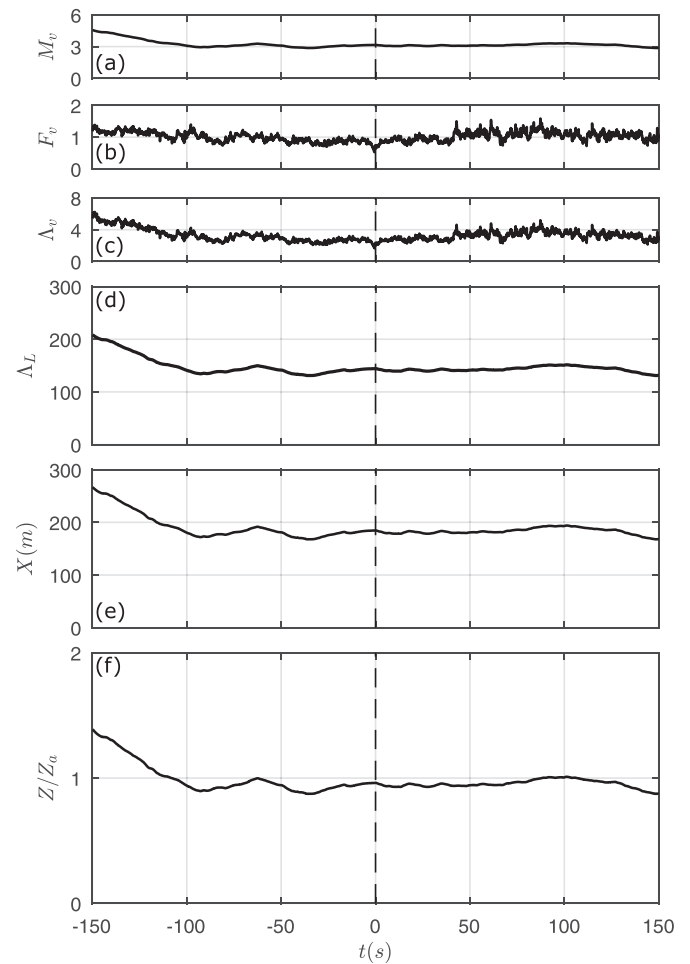Fig. 19. Same as Fig. 18, but for the anemometer LI.03.

Fig. 20. Same as Figs. 18 and 19, but for the anemometer LI.05.

Holmes et al., 2008; Pistotnik et al., 2011). Second, the absence of the second downburst peak in the proper m record is also noticeable. In other words, the overall structure of the m times series is much simpler that of the p series, which is expected since the real environment is characterized with a number of complexities which are not accounted for in the idealized physical or numerical simulations. However, despite these discrepancies there is still a high level of correlation between the instantaneous p and m velocity records of this event (Table 2).

Quantitatively, however, γ functions centered around the main downburst peak of the p and m events are very similar (Fig. 16) with the RMSE = 0.08126 and $r_\gamma = 0.936$ between two time series. The good match between γ functions is due to the imposed restriction of the method to analyze only the behavior of the γ functions around the first downburst peak (i.e., 5-min around the peak). Therefore, the matching between the p and m records is inspected only by taking into account the main downburst signature and not the overall properties of the time series because the m records lack some of the secondary features of real downburst; as discussed above.

Time series of $\tilde{v}_m'$ deviates from the random Gaussian process (Fig. 17b) in the region around the ramp-up and the velocity peak. This finding indicates that this segment of the time series might be considered as deterministic when compared to the rest of the record. However, similar feature is not observed in the p record (Fig. 17a). However, although $\tilde{v}'$ records have similar values of skewness and kurtosis, Fig. 17d demonstrates higher degree of non-Gaussianity of $\tilde{v}_m'$.

The mean part of the velocity scale, $M_v(T_m)$, in Fig. 18a shows the typically observed decreasing trend in the first 50 s due to the mismatch between the background ABL winds in p and m records. The velocity

scale, $\Lambda_v(T_m)$, in Fig. 18c is similar to its mean part, $M_v(T_m)$, because the fluctuating component, $F_v(T_m)$, is almost constant and equal to unity. The resulting length scale of this event at the location of anemometer LI.01 is approximately 100:1 (Fig. 18d). Fig. 18e and f depict the estimated radial position of the p downburst center in respect to the anemometer LI.01 [Eq. (23)] and the anemometer height AGL [Eq. (22)], respectively. The same analysis, but for the anemometers LI.03 and LI.05 are shown in Fig. 19 and Fig. 20, respectively. These plots demonstrate the effectiveness of the proposed method as the evaluated heights of the anemometers from the obtained kinematic and geometric scales closely match the real anemometer heights. The heights of the anemometers LI.03 and LI.05 are 25 m and 75 m AGL (Table 1), respectively, while the proposed scaling method estimates their heights to be around 20 m (Figs. 19f) and 74 m AGL (Fig. 20f), respectively. For the anemometer LI.01 the estimated height is about 30 m AGL, while in reality the anemometer is positioned at 25 m AGL (Table 1).

This partial reconstruction of the p event from Livorno shows that the downburst center was probably approximately 400 m southwest from anemometer LI.01 (Fig. 21). The azimuthal direction of downburst center is obtained by knowing the wind direction at the time instant of maximum wind velocity (Table 1). The northward to northeastward movement of downburst as well as different downburst diameters at the time of the maximum wind speed at each of three anemometers are portrayed in Fig. 21. It is important to note that the same p event captured with multiple anemometers, such as this Livorno event, has different m matches in the WindEEE Dome (i.e., different R/D and Z/D positions). This is because p downbursts are: (1) embedded into background ABL winds that can have pronounced velocity sheer with height; (2)
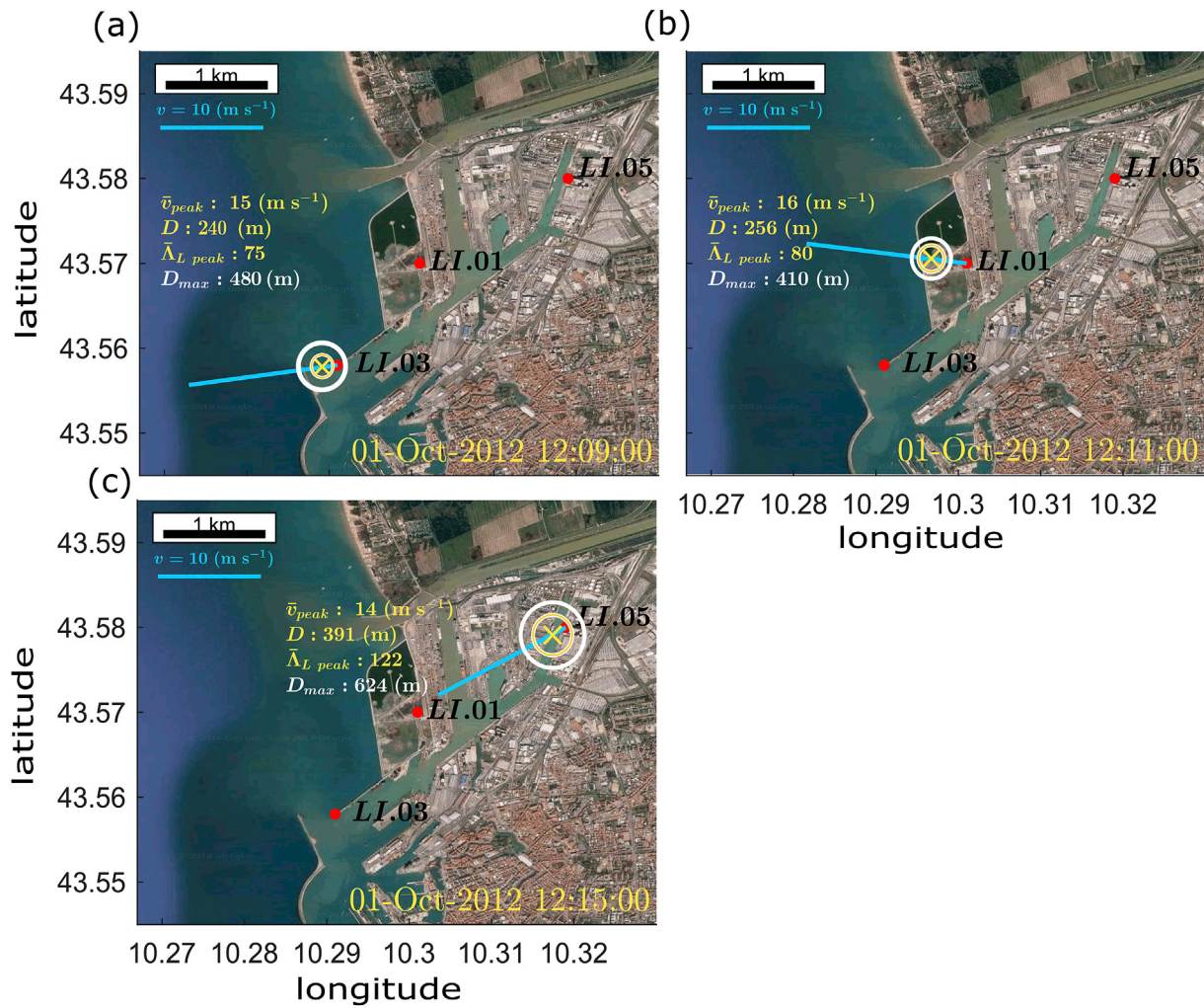
Fig. 21. Estimated position of the p downburst center (yellow ×) at the time instant of the peak velocity (Livorno, 1 October 2012, all three anemometers). The red dot is anemometer position, D is the estimated downburst diameter (yellow circle) while D_{max} is the estimated distance between downburst center and the maximum wind speed in downburst outflow (white circle). The blue line indicates wind speed and direction at the time instant of peak velocity. (For interpretation of the references to colour in this figure legend, the reader is referred to the Web version of this article.)

translating together with the parent thunderstorm cloud; (3) interact with changing surface roughness (albeit this effect is small in the analyzed p cases); (4) buoyancy-driven phenomena that depends on atmospheric stability; and (5) dependent on the life-cycle of the parent cloud. Therefore the m downburst can be viewed as the static impinging jets equivalent to the p events at particular R/D and Z/D positions. That is, the entire m event in spatiotemporal terms is not necessarily the entire p event. Although this is a limitation of the physical experiments, it is currently not possible to accurately simulate all the complexities of p downbursts in the wind simulator. These limitations are further discussed in Section 5. However, the effectiveness of the proposed scaling method is demonstrated by the accurate prediction of real anemometer heights.

5. Conclusions and future research

This study introduces a novel scaling technique of downburst outflows aiming to reproduce specific downbursts detected at the full-scale, or families of these, in an experimental facility. Scaling of downburst events is a key aspect of wind engineering, both with regard to laboratory simulation of the flow as well as to the investigation of downburst wind loading, wind-induced response and aeroelastic effects on structures.

The proposed method compares the γ functions of modelled downbursts in a wind simulator (m downbursts) and full scale downburst events (p downbursts). The γ function, defined as a ratio $\bar{v}_s / \bar{v}_{\max,s}$ (where

$\bar{v}_s$ is the slowly-varying mean, $\bar{v}_{\max,s}$ is the maximum value of $\bar{v}_s$, and s is either p or m), describes in non-dimensional form the highly transient downburst time series characterized by velocity ramp-up, peak, and slowdown of wind speed. The best match between γ_p and γ_m is obtained through a parametric procedure which finds the best averaging window of m data. The whole scaling methodology is described in details in Section 2.

The scaling method was tested on 1400 m downburst records experimentally simulated in the Wind Engineering, Energy and Environment (WindEEE) Dome (Hangan et al., 2017) at Western University in Canada, and on 17 p records from the Mediterranean in Italy. The p downbursts are measured under the scope of the European project "Wind and Ports" (Solari et al., 2012). This dataset is the largest collection of p and m downbursts analyzed so far.

First, the simulated downbursts in the WindEEE Dome closely resemble the transient features of p downbursts both qualitatively and quantitatively. This similarity is demonstrated by comparing the γ functions of p and m records and by inspecting their slope and symmetry for different averaging times. In addition, the μ functions ($\mu_s(t_s) = I_{v,s}(t_s)/\bar{I}_{v,s}$; where $I_{v,s}(t_s)$ is the slowly-varying turbulence intensity in time t_s, and $\bar{I}_{v,s}$ is its mean value) between p and m records are also analyzed and their similarity is confirmed. While γ describe the mean feature of the flow, the μ functions describe the fluctuating (turbulent) properties of

downburst outflows. It was concluded that each γ function can be represented as a sample of a highly transient random process, whereas the μ functions are quasi-stationary and deterministic.

Second, the typical velocity and time scales between the investigated p and m records are found to be between 2:1 to 4:1 and 40:1 to 70:1, respectively. However, significant deviations from these values are also observed. The resulting length scales are obtained as the product of velocity and time scales and they are in typically around 100:1 to 250:1, and similar.

Third, the proposed scaling method is validated on several p downburst events, but only two are shown in this study—one from Genoa, Italy, that occurred on 30 September 2012 and the other from Livorno, Italy, that took place on 1 October 2012. The Genoa event was recorded with one anemometer, while the Livorno event was captured by three anemometers. The proposed scaling method accurately predicted the height of the anemometers to be around 13 m above ground level (AGL) in Genoa and at around 25 and 74 m AGL in Livorno. In addition, the scaling method enabled a partial reconstruction of the selected p events in terms of evaluating the radial distance of downburst touchdown and the radius of the maximum wind speed in the downburst outflow in respect to the anemometer positions. In all investigated cases, the downbursts were spawned above the sea and advanced toward the coast.

At the end, it is important to discuss a couple of caveats and limitations of the proposed method, as well as to highlight the prospects for its further improvements. Two biggest limitations of this scaling method are: (1) not accounting for the existence of background atmospheric boundary layer (ABL) winds; and (2) the scaling is not based on the entire flow field, but on the signal properties of point measurements in the p and m events. These challenges are often faced in the scaling methodologies proposed in other studies (e.g., Wood et al., 2001; Chay and Letchford, 2002; McConville et al., 2009). The first issue can be partially resolved by producing downbursts and ABL winds at the same time in a wind simulator. Yet another approach to tackle this challenge is to simply subtract the background ABL winds from the p records and then the modified p time series could be compared against the m records. This exercise was carried out (results not shown) and it resulted in a larger time and velocity scales (also consequently larger length scales) between the p and m events. However, the matching of anemometer heights was less accurate. These results are not shown here because simple addition/subtraction of downburst and ABL winds tends to be physically inaccurate as recently demonstrated by Romanic and Hangan (2018) and Romanic et al. (2019). Namely, the interaction between these two flows depends on the radial position of the anemometer in respect to downburst center, the direction of incoming ABL wind, as well as the anemometer height, among a number of other factors. Since an established methodology for this decomposition does not exist at the moment, it would be impossible to estimate the introduced error in the modified p records and consequently the inaccuracy of obtained scales.

The second challenge listed above is somewhat related to the previous discussion. Namely, in order to completely replicate a p event in a wind simulator, the m time series need to account for the background ABL winds, cloud translation, and potential surface roughness changes (excluding the atmospheric stability from this list), as well as the close anemometer surrounding. If these requirements are accurately achieved in a wind simulator then the argument can be made that the entire flow fields of p and m events are similar. However, this level of precision is currently not obtained in any of the existing physical simulators. It could be achieved by means of numerical simulations carried out with cloud models (see for instance Oreskovic et al., 2018) but this very promising practice is still at the frontier in this research field. T The proposed method in this paper as well as other more simplistic scaling methodologies, potentially provide an equivalent scale that a stationary m downburst without ABL winds would have in order to replicate the translating p downburst embedded in the background ABL winds. However, other methodologies that attempt to reconstruct downburst outflow without creating an impinging jet downdraft have also been put forward (Jesson

et al., 2019; Aboutabikh et al., 2019), which altogether demonstrates that this topic still deserves more research.

References

Aboutabikh, M., Ghazal, T., Chen, J., Elgamal, S., Aboshosha, H., 2019. Designing a blade-system to generate downburst outflows at boundary layer wind tunnel. J. Wind Eng. Ind. Aerodyn. 186, 169–191. https://doi.org/10.1016/j.jweia.2019.01.005.

Bakke, P., 1957. An experimental investigation of a wall jet. J. Fluid Mech. 2, 467–472. https://doi.org/10.1017/S0022112057000270.

Burlando, M., Romanić, D., Solari, G., Hangan, H., Zhang, S., 2017. Field data analysis and weather scenario of a downburst event in Livorno. Mon. Weather Rev. 145, 3507–3527. https://doi.org/10.1175/MWR-D-17-0018.1. Italy, on 1 October 2012.

Burlando, M., Zhang, S., Solari, G., 2018. Monitoring, cataloguing and weather scenarios of thunderstorm-induced intense wind events. Nat. Hazards Earth Syst. Sci. 18, 2309–2330. https://doi.org/10.5194/nhess-18-2309-2018.

Charba, J., 1974. 1974. Application of gravity current model to analysis of squall-line gust front, 10.1175/1520-0493 Mon. Weather Rev. 102, 140–156, 102<0140: AOGCMT>2.0.CO;2.

Chay, M.T., Letchford, C.W., 2002. Pressure distributions on a cube in a simulated thunderstorm downburst—Part A: stationary downburst observations. J. Wind Eng. Ind. Aerodyn. 90, 711–732. https://doi.org/10.1016/S0167-6105(02)00158-7.

Chen, L., Letchford, C.W., 2006. Multi-scale correlation analyses of two lateral profiles of full-scale downburst wind speeds. J. Wind Eng. Ind. Aerodyn. 94, 675–696. https://doi.org/10.1016/j.jweia.2006.01.021.

Choi, E.C., Hidayat, F.A., 2002. Dynamic response of structures to thunderstorm winds. Prog. Struct. Mater. Eng. 4, 408–416, 10.1002/pse.132.

De Gaetano, P., Repetto, M.P., Repetto, T., Solari, G., 2014. Separation and classification of extreme wind events from anemometric records. J. Wind Eng. Ind. Aerodyn. 126, 132–143. https://doi.org/10.1016/j.jweia.2014.01.006.

Fujita, T.T., 1985. The Downburst: Microburst and Macroburst. Satellite and Mesometeorology Research Project, Department of the Geophysical Sciences. University of Chicago, Chicago, Illinois, United States.

Fujita, T.T., 1990. Downbursts: meteorological features and wind field characteristics. J. Wind Eng. Ind. Aerodyn. 36, 75–86. https://doi.org/10.1016/0167-6105(90) 90294-M.

Gast, K.D., Schroeder, S., 2004. Extreme wind events observed in the 2002 thunderstorm outflow experiment. 22nd conference on severe local storms. In: Paper Presented at the 11th Conference on Aviation, Range, and Aerospace and the 22nd Conference on Severe Local Storms. American Meteorological Society. Massachusetts, United States, Boston.

Hangan, H., 2010. Current and future directions for wind research at Western: a new quantum leap in wind research through the Wind Engineering, Energy and Environment (WindEEE) Dome. Wind Engineers. JAWE 35, 277–281, 10.5359/ jawe.35.277.

Hangan, H., Refan, M., Jubayer, C., Romanic, D., Parvu, D., LoTufo, J., Costache, A., 2017. Novel techniques in wind engineering. J. Wind Eng. Ind. Aerodyn. 171, 12–33, 10.1016/j.jweia.2017.09.010.

Hangan, H., Romanic, D., Jubayer, C., 2019. Three-dimensional, non-stationary and non-Gaussian (3D-NS-NG) wind fields and their implications to wind–structure interaction problems. J. Fluid Struct. https://doi.org/10.1016/ j.jfluidstructs.2019.01.024.

Hjelmfelt, M.R., 1988. Structure and life cycle of microburst outflows observed in Colorado. J. Appl. Meteorol. 27, 900–927, 10.1175/1520-0450(1988)027 <0900: SALCOM>2.0.CO;2.

Ho, T.C.E., Surry, D., Morrish, D., Kopp, G.A., 2005. The UWO contribution to the NIST aerodynamic database for wind loads on low buildings: Part 1. Archiving format and basic aerodynamic data. J. Wind Eng. Ind. Aerodyn. 93, 1–30. https://doi.org/ 10.1016/j.jweia.2004.07.006.

Holmes, J.D., 2002. A re-analysis of recorded extreme wind speeds in Region A. Aust. J. Struct. Eng. 4, 29–40. https://doi.org/10.1080/13287982.2002.11464905.

Holmes, J., Oliver, S., 2000. An empirical model of a downburst. Eng. Struct. 22, 1167–1172. https://doi.org/10.1016/S0141-0296(99)00058-9.

Holmes, J.D., Hangan, H.M., Schroeder, J.L., Letchford, C.W., Orwig, K.D., 2008. A forensic study of the Lubbock-Reese downdraft of 2002. Wind Struct. 11, 137–152. https://doi.org/10.12989/was.2008.11.2.137.

Järvi, L., Punkka, A.-J., Schultz, D.M., Petäjä, T., Hohti, H., Rinne, J., Pohja, T., Kulmala, M., Hari, P., Vesala, T., 2007. Micrometeorological observations of a microburst in southern Finland. Bound-Lay. Meteorol 125, 343–359. https://doi.org/10.1007/s10546-007-9204-7.

Jesson, M., Sterling, M., 2018. A simple vortex model of a thunderstorm downburst – a parametric evaluation. J. Wind Eng. Ind. Aerodyn. 174, 1–9. https://doi.org/10.1016/j.jweia.2017.12.001.

Jesson, M., Lombardo, F.T., Sterling, M., Baker, C., 2019. The physical simulation of a transient, downburst-like event – how complex does it need to be? J. Wind Eng. Ind. Aerodyn. 189, 135–150. https://doi.org/10.1016/j.jweia.2019.03.021.

Jones, C.S., Cenedese, C., Chassignet, E.P., Linden, P.F., Sutherland, B.R., 2015. Gravity current propagation up a valley. J. Fluid Mech. 762, 417–434. https://doi.org/10.1017/jfm.2014.627.

Junayed, C.J., Jubayer, C., Parvu, D., Romanic, D., Hangan, H., 2019. Flow field dynamics of large-scale experimentally produced downburst flows. J. Wind Eng. Ind. Aerodyn. 188, 61–79. https://doi.org/10.1016/j.jweia.2019.02.008.

Kim, J., Hangan, H., 2007. Numerical simulations of impinging jets with application to downbursts. J. Wind Eng. Ind. Aerodyn. 95, 279–298. https://doi.org/10.1016/j.jweia.2006.07.002.

Kwon, D., Kareem, A., 2009. 2009. Gust-front factor: new framework for wind load effects on structures. J. Struct. Eng. 135, 717–732. https://doi.org/10.1061/(ASCE)0733-9445, 135:6(717).

Letchford, C.W., Chay, M.T., 2002. Pressure distributions on a cube in a simulated thunderstorm downburst. Part B: moving downburst observations. J. Wind Eng. Ind. Aerodyn. 90, 733–753. https://doi.org/10.1016/S0167-6105(02)00163-0.

Letchford, C., Illidge, G.C., 1999. Turbulence and topographic effects in simulated thunderstorm downdrafts by wind tunnel jet. In: Larsen, A., Larose, G., Livesey, F. (Eds.), Proceedings of the Tenth International Conference on Wind Engineering. Paper Presented at the Wind Engineering into the 21st Century. A. A. Balkema: Copenhagen, Denmark, 1907–1912.

Letchford, C., Mans, C., Chay, M., 2002. Thunderstorms—their importance in wind engineering (a case for the next generation wind tunnel). J. Wind Eng. Ind. Aerodyn. 90, 1415–1433. https://doi.org/10.1016/S0167-6105(02)00262-3.

Linden, P., 2012. Gravity currents—theory and laboratory experiments. In: Cenedese, C., Chassignet, E.P., Verron, J. (Eds.), Buoyancy-Driven Flows. Cambridge University Press, Cambridge, England, pp. 13–51. https://doi.org/10.1017/CBO9780511920196.002.

Lombardo, F.T., Smith, D.A., Schroeder, J.L., Mehta, K.C., 2014. Thunderstorm characteristics of importance to wind engineering. J. Wind Eng. Ind. Aerodyn. 125, 121–132. https://doi.org/10.1016/j.jweia.2013.12.004.

Lompar, M., Ćurić, M., Romanic, D., 2018. Implementation of a gust front head collapse scheme in the WRF numerical model. Atmos. Res. 203, 231–245. https://doi.org/10.1016/j.atmosres.2017.12.018.

Lundgren, T.S., Yao, J., Mansour, N.N., 1992. Microburst modelling and scaling. J. Fluid Mech. 239, 461–488. https://doi.org/10.1017/S002211209200449X.

Mahoney, W.P., 1988. Gust front characteristics and the kinematics associated with interacting thunderstorm outflows. Mon. Weather Rev. 116, 1474–1492. https://doi.org/10.1175/1520-0493(1988)116<1474:GFCATK>2.0.CO;2.

Mason, M.S., Wood, G.S., 2005. Influence of Jet Inclination on Structural Loading in an Experimentally Simulated Microburst. Paper Presented at the 6th Asia-Pacific Conference on Wind Engineering. South Korea, Seoul.

Mason, M.S., Letchford, C.W., James, D.L., 2005. Pulsed wall jet simulation of a stationary thunderstorm downburst, Part A: physical structure and flow field characterization. J. Wind Eng. Ind. Aerodyn. 93, 557–580. https://doi.org/10.1016/j.jweia.2005.05.006.

McConville, A.C., Sterling, M., Baker, C.J., 2009. The physical simulation of thunderstorm downbursts using an impinging jet. Wind Struct. 12, 133–149. https://doi.org/10.12989/was.2009.12.2.133.

McCullough, M., Kwon, D.K., Kareem, A., Wang, L., 2014. Efficacy of averaging interval for nonstationary winds. J. Eng. Mech. 140, 1–19. https://doi.org/10.1061/(ASCE)EM.1943-7889.0000641.

Nasr-Azadani, M.M., Meiburg, E., 2016. Gravity currents propagating into ambients with arbitrary shear and density stratification: vorticity-based modelling. Q. J. Royal Meteorol. Soc. 142, 1359–1370. https://doi.org/10.1002/qj.2739.

Oreskovic, C., Orf, L.G., Savory, E., 2018. A parametric study of downbursts using a full-scale cooling source model. J. Wind Eng. Ind. Aerodyn. 180, 168–181.

Pistotnik, G., Holzer, A.M., Kaltenböck, R., Tschannett, S., 2011. An F3 downburst in Austria—a case study with special focus on the importance of real-time site surveys. Atmos. Res. 100, 565–579. https://doi.org/10.1016/j.atmosres.2010.10.011.

Poreh, M., Tsuei, Y.G., Cermak, J.E., 1967. Investigation of a turbulent radial wall jet. J. Appl. Mech. 34 (457), 10.1115/1.3607705.

Potter, M.C., Wiggert, D.C., Ramadan, B.H., 2011. Mechanics of Fluids. Cengage Learning, Boston, Massachusetts, United States.

Refan, M., Hangan, H., Wurman, J., 2014. Reproducing tornadoes in laboratory using proper scaling. J. Wind Eng. Ind. Aerodyn. 135, 136–148. https://doi.org/10.1016/j.jweia.2014.10.008.

Repetto, M.P., Burlando, M., Solari, G., De Gaetano, P., Pizzo, M., Tizzi, M., 2018. A web-based GIS platform for the safe management and risk assessment of complex structural and infrastructural systems exposed to wind. Adv. Eng. Softw. 117, 29–45. https://doi.org/10.1016/j.advengsoft.2017.03.002.

Romanic, D., Hangan, H., 2018. In: The Interplay between Background Atmospheric Boundary Layer Winds and Downburst Outflows. A First Physical Experiment. Proceedings of the XV Conference of the Italian Association for Wind Engineering (IN-VENTO 2018). Elsevier, Napoli, Italy.

Romanic, D., LoTufo, J., Hangan, H., 2019. Transient behavior in impinging jets in crossflow with application to downburst flows. J. Wind Eng. Ind. Aerodyn. 184, 209–227. https://doi.org/10.1016/j.jweia.2018.11.020.

Simpson, J.E., 1969. A comparison between laboratory and atmospheric density currents. Q. J. Royal Meteorol. Soc. 95, 758–765. https://doi.org/10.1002/qj.49709540609.

Simpson, J.E., 1972. Effects of the lower boundary on the head of a gravity current. J. Fluid Mech. 53, 759–768. https://doi.org/10.1017/S0022112072000461.

Simpson, J.E., Britter, R.E., 1980. A laboratory model of an atmospheric mesofront. Q. J. Royal Meteorol. Soc. 106, 485–500. https://doi.org/10.1002/qj.49710644907.

Solari, G., Repetto, M.P., Burlando, M., De Gaetano, P., Pizzo, M., Tizzi, M., Parodi, M., 2012. The wind forecast for safety management of port areas. J. Wind Eng. Ind. Aerodyn. 104–106, 266–277. https://doi.org/10.1016/j.jweia.2012.03.029.

Solari, G., Burlando, M., De Gaetano, P., Repetto, M.P., 2015a. Characteristics of thunderstorms relevant to the wind loading of structures. Wind Struct. 20, 763–791. https://doi.org/10.12989/was.2015.20.6.763.

Solari, G., De Gaetano, P., Repetto, M.P., 2015b. Thunderstorm response spectrum: fundamentals and case study. J. Wind Eng. Ind. Aerodyn. 143, 62–77. https://doi.org/10.1016/j.jweia.2015.04.009.

Wakimoto, R.M., 1982. 1982. The life cycle of thunderstorm gust fronts as viewed with Doppler radar and rawinsonde data. Mon. Weather Rev. 110, 1060–1082. https://doi.org/10.1175/1520-0493, 110<1060:TLCOTG>2.0.CO;2.

Wakimoto, R.M., 1985. 1985. Forecasting dry microburst activity over the High Plains Mon. Weather Rev. 113, 1131–1143. https://doi.org/10.1175/1520-0493, 113<1131:FDMAOT>2.0.CO;2.

Walker, J.D.A., Smith, C.R., Cerra, A.W., Doligalski, T.L., 1987. The impact of a vortex ring on a wall. J. Fluid Mech. 181, 99–140. https://doi.org/10.1017/S0022112087002027.

Wood, G.S., Kwok, K.C., Motteram, N.A., Fletcher, D.F., 2001. Physical and numerical modelling of thunderstorm downbursts. J. Wind Eng. Ind. Aerodyn. 89, 535–552. https://doi.org/10.1016/S0167-6105(00)00090-8.

Xu, Z., Hangan, H., 2008. Scale, boundary and inlet condition effects on impinging jets. J. Wind Eng. Ind. Aerodyn. 96, 2383–2402. https://doi.org/10.1016/j.jweia.2008.04.002.

Zhang, S., Solari, G., De Gaetano, P., Burlando, M., Repetto, M.P., 2017. A refined analysis of thunderstorm outflow characteristics relevant to the wind loading of structures. Probabilist. Eng. Mech 54, 9–24. https://doi.org/10.1016/j.probengmech.2017.06.003.